2011

The CO-H2 Conversion Factor in Disc Galaxies and Mergers

Desika Narayanan
Haverford College, dnarayan@haverford.edu

Monthly Notices
of the
ROYAL ASTRONOMICAL SOCIETY

Mon. Not. R. Astron. Soc. **418,** 664–679 (2011) doi:10.1111/j.1365-2966.2011.19516.x

The CO–H_2 conversion factor in disc galaxies and mergers

Desika Narayanan,[1]★† Mark Krumholz,[2] Eve C. Ostriker[3] and Lars Hernquist[4]

[1]*Steward Observatory, University of Arizona, 933 N Cherry Ave, Tucson, AZ 85721, USA*
[2]*Department of Astronomy and Astrophysics, University of California, Santa Cruz, CA 95064, USA*
[3]*Department of Astronomy, University of Maryland, College Park, MD 20742, USA*
[4]*Harvard-Smithsonian Center for Astrophysics, 60 Garden St., Cambridge, MA 02138, USA*

Accepted 2011 July 26. Received 2011 July 22; in original form 2011 April 20

ABSTRACT

Relating the observed CO emission from giant molecular clouds (GMCs) to the underlying H_2 column density is a long-standing problem in astrophysics. While the Galactic CO–H_2 conversion factor (X_{CO}) appears to be reasonably constant, observations indicate that X_{CO} may be depressed in high surface density starburst environments. Using a multiscale approach, we investigate the dependence of X_{CO} on the galactic environment in numerical simulations of disc galaxies and galaxy mergers. X_{CO} is proportional to the GMC surface density divided by the integrated CO intensity, W_{CO}, and W_{CO} is related to the kinetic temperature and velocity dispersion in the cloud. In disc galaxies (except within the central $\sim$ kpc), the galactic environment is largely unimportant in setting the physical properties of GMCs provided they are gravitationally bound. The temperatures are roughly constant at $\sim$10 K due to the balance of CO cooling and cosmic ray heating, giving a nearly constant CO–H_2 conversion factor in discs. In mergers, the velocity dispersion of the gas rises dramatically during coalescence. The gas temperature also rises as it couples well to the warm ($\sim$50 K) dust at high densities ($n > 10^4$ cm^{-3}). The rise in velocity dispersion and temperature combine to offset the rise in surface density in mergers, causing X_{CO} to drop by a factor of $\sim$2–10 compared to the disc simulation. This model predicts that high-resolution Atacama Large Millimeter/submillimeter Array observations of nearby ultraluminous infrared galaxies should show velocity dispersions of 10^1–10^2 km s^{-1}, and brightness temperatures comparable to the dust temperatures.

Key words: ISM: clouds – ISM: molecules – galaxies: interactions – galaxies: ISM – galaxies: starburst – galaxies: star formation.

1 INTRODUCTION

Stars form in giant molecular clouds (GMCs) whose primary constituent is molecular hydrogen, H_2. Because H_2 lacks a permanent dipole moment, and the lowest lying excited state capable of quadrupole emission requires temperatures $\sim$500 K to be excited, the physical conditions in the cold ($\sim$10 K) molecular gas are typically probed via tracer molecules, rather than by direct detection of H_2.

Carbon monoxide ($^{12}C^{16}O$; hereafter CO) is the second most abundant molecule in GMCs. Because the $J = 1$–0 rotational transition of CO lies only $\sim$5 K above ground, has a relatively low effective density ($\sim 10^{2-3}$ cm^{-3}) for excitation (Evans 1999), and has a wavelength of $\sim$3 mm which is readily observable from the ground, CO ($J = 1$–0) has historically been one of the most commonly used tracers of physical conditions in the molecular interstellar medium (ISM).

A large uncertainty in using CO to trace H_2 gas is relating the observed CO line luminosity to the underlying H_2 column density. However, despite the fact that CO/H_2 abundances vary strongly within GMCs (e.g. Sternberg & Dalgarno 1995; Lee, Bettens & Herbst 1996; Hollenbach & Tielens 1999; Glover et al. 2010; Glover & Mac Low 2011), a multitude of observations suggests that the conversion factor between CO and H_2 is reasonably constant in Galactic GMCs, following the relation:

$$X_{CO} = 2\text{–}4 \times 10^{20}\,\mathrm{cm^{-2}/(K\,km\,s^{-1})}, \quad (1)$$

where X_{CO} is the CO–H_2 conversion factor in units of H_2 column density divided by velocity-integrated CO line intensity.[1] Lines of evidence for a relatively constant X_{CO} include comparisons between CO luminosities and molecular column densities determined

★E-mail: dnarayanan@as.arizona.edu
†Bart J. Bok Fellow.

[1] X_{CO} is sometimes referred to in the literature as the 'X-factor'. We will use X_{CO} and X-factor interchangeably.

via a variety of techniques, including dust extinction (Dickman 1975), γ-ray emission (Bloemen et al. 1986; Strong & Mattox 1996; Abdo et al. 2010b) and thermal dust emission (Dame, Hartmann & Thaddeus 2001; Draine et al. 2007).

Beyond this, the CO–H_2 conversion factor appears to have the same relatively narrow range of values in galaxies in the Local Group as well (Blitz et al. 2007; Wolfire, Hollenbach & McKee 2010), though there may be some variations associated with metallicity (Wilson 1995; Arimoto, Sofue & Tsujimoto 1996; Boselli, Lequeux & Gavazzi 2002; Rosolowsky et al. 2003; Israel 2005; Bell et al. 2006; Leroy et al. 2006, 2011; Bell, Viti & Williams 2007; Bolatto et al. 2008). The relatively narrow distribution of values for X_{CO} in Local Group GMCs[2] may arise from the fact that molecular clouds appear have remarkably similar physical properties in both the Milky Way and nearby galaxies. GMCs in the Galaxy and local Universe appear to have a nearly constant surface density of 85–100 $M_\odot$ pc^{-2}, obey the size–linewidth relation and have relatively low kinetic temperatures of 10–20 K (Solomon et al. 1987; Blitz et al. 2007; Heyer et al. 2009). Magnetohydrodynamic (MHD) and radiative transfer modelling by Glover et al. (2010), Glover & Mac Low (2011) and Shetty et al. (2011a,b) have shown that simulated GMCs with mean densities, sizes, velocity dispersions and metallicities comparable to those found in the Galaxy naturally produce X_{CO} conversion factors comparable to equation (1).

The situation becomes more complex in starburst galaxies. By utilizing high spatial resolution interferometric mapping of nearby ultraluminous infrared galaxies (ULIRGs; $L_{IR} > [10^{12}]10^{11}$ $L_\odot$), Solomon et al. (1997) and Downes & Solomon (1998, 2003) have shown that the application of the 'standard' Galactic X_{CO} conversion factor would cause the inferred molecular gas mass to exceed the dynamical mass in these galaxies. In this case, the constraints on X_{CO} are in the range $\sim$2–10 $\times$ 10^{19} cm^{-2}/K km s^{-1}: a factor of 2–20 lower than the Galactic value. Other observational evidence from local starbursts (Hinz & Rieke 2006; Meier et al. 2010), the Galactic Centre (Oka et al. 1998) and high-z submillimetre galaxies (Tacconi et al. 2008) have all corroborated this picture that X_{CO} may be lower in regions of high molecular surface density.

The exact origin of a lower X_{CO} factor in starburst galaxies is not entirely clear. Models by Maloney & Black (1988) which predate the aforementioned observations, predicted that warmer molecular gas temperatures in infrared-luminous galaxies may drive a lower X_{CO} conversion factor due to an increase in CO brightness temperature with kinetic temperature in optically thick clouds. Alternatively, Downes & Solomon (1998) suggest that the CO linewidth in starbursts traces a combination of the gaseous and stellar potential, rather than just the H_2 mass. In the case where CO is optically thick, the observed velocity-integrated CO line intensity can increase with the velocity dispersion. Maloney & Black (1988) and Shetty et al. (2011b) also postulated a similar effect if the CO linewidths were larger than their typical virial values.

While the scaling of X_{CO} with environmental parameters is not yet known, the ramifications are profound. For example, if X_{CO} does indeed systematically vary in higher surface density environments, our current understanding of the normalization and index of the Kennicutt–Schmidt (KS) star formation rate (SFR)–gas surface density relation in star-forming galaxies may change (Kennicutt 1998a; Daddi et al. 2010; Genzel et al. 2010). At higher redshifts, as high gas surface density galaxies begin to contribute substantially to the cosmic SFR density (e.g. Le Floc'h et al. 2005; Hopkins et al. 2010; Hopkins & Hernquist 2010), the variation of X_{CO} with environment may affect observed values of the cosmic evolution of Ω_{H_2}. More generally, the interpretation of forthcoming results from the Expanded Very Large Array (EVLA) and Atacama Large Millimeter/submillimeter Array (ALMA) will be severely crippled without an understanding for how to relate the observed CO line flux to the quantity of interest: H_2 gas mass.

In this area, numerical simulations can offer some guidance. Indeed, understanding the origin of X_{CO} in galaxies is difficult in that many of the physical parameters driving the relation are coupled. The CO–H_2 conversion factor, X_{CO}, has dimensions of

$$X_{CO} \propto \Sigma/(W_{CO}) \propto \Sigma/(\sigma T_B), \quad (2)$$

where W_{CO} is the velocity-integrated CO intensity, Σ is the gas surface density, T_B is the brightness temperature of the line and σ is the velocity dispersion. To first order, T_B is related to the kinetic temperature of the gas (T_k) when the line is thermalized. However, the kinetic temperature of the gas can depend on molecular abundances, gas densities, dust temperatures and the background radiation field (e.g. Narayanan et al. 2006b; Krumholz, Leroy & McKee 2011). The same physical processes which can cause changes in these parameters may also cause the GMC surface densities to change as well. The problem is well suited for numerical simulations.

Building on the seminal work of Maloney & Black (1988) and more recent simulations of Glover et al. (2010), Glover & Mac Low (2011) and Shetty et al. (2011a,b), we present the first models investigating the CO–H_2 conversion factor in hydrodynamic simulations of isolated disc galaxies and disc galaxy mergers. This is the first paper in a series. In this work, we aim to understand whether X_{CO} varies between 'normal' disc galaxies and galaxy mergers, and if so, why. In order to do this, we couple smoothed particle hydrodynamic (SPH) simulations of galaxies in evolution with dust and molecular line radiative transfer calculations to self-consistently calculate the kinetic temperature of and emissivity from GMCs in our models. Our main result is that higher kinetic temperatures and velocity dispersions in the GMCs naturally arise during mergers, and contribute to lower values of X_{CO} in these systems.

Our paper is organized as follows: in Section 2, we present our radiative transfer and hydrodynamics methodology; in Section 3, we discuss the synthetic observational and physical properties of our model galaxies in an effort to aid comparisons to observations; in Section 4, we discuss how the CO–H_2 conversion factor varies in disc galaxies and mergers in our models; in Section 5, we discuss the implications of our findings and in Section 6, we summarize our results.

2 METHODS

Our goal is to simulate the emission from GMCs on galaxy-wide scales. This involves simulating galaxies in evolution, the physical state of GMCs, molecular line radiative transfer through the clouds and dust and molecular line radiative transfer through the galaxy. In this section, we describe these simulations, and the relevant assumptions that go into our modelling. This involves combining a large number of simulation codes. In light of this, to guide the reader through the numerical details and equations in this section, we first summarize them more generally here.

[2] X_{CO} also appears to be reasonably constant in diffuse H_2 gas in the Galaxy (Liszt, Pety & Lucas 2010). This has been attributed to the offsetting effects of lower CO abundances with respect to H_2 (most of the carbon is in C^+) and a large W_{CO}/N_{CO} ratio in low extinction gas. See the discussion in Pety, Liszt & Lucas (2011) for more details.

We first simulate the hydrodynamic evolution of both disc galaxies and mergers. It is from these simulations that we know the global distribution of stars, gas and metals in the galaxy, and their physical properties. The radiative transfer occurs in post-processing. We project the physical conditions of the particles on to an adaptive mesh using the SPH smoothing kernel. The base mesh is 5^3 spanning a 200-kpc box. The cells refine recursively into 2^3 subcells based on the refinement criteria the relative density variations of metals ($\sigma_{\rho_m}/\langle\rho_m\rangle$) should be less than 0.1, and the V-band optical depth across a cell be less than unity. The maximum refinement level was 11, such that the smallest cells in this mesh are of order $\sim$70 pc across.

The surface density of and velocity dispersion within the GMCs are set by the physical conditions in the hydrodynamic galaxy evolution simulations. A subgrid prescription comes into play when GMCs are unresolved (i.e. when cells in the adaptive mesh are very large). We assume that all of the H_2 mass in the cell is in the GMC and we calculate the H I–H_2 balance via analytic models (described below). From this, the complete physical conditions (except for the temperature) of the GMCs are described by the hydrodynamic galaxy evolution simulations. The temperatures of the clouds are calculated by assuming thermal equilibrium between gas heating (by the grain photoelectric effect and cosmic rays), gas cooling (via molecular and atomic line cooling), dust heating (from the ambient radiation field), thermal dust cooling and some energy exchange between gas and dust.

With the physical properties of the galaxies and GMCs known, we then proceed to calculate the emergent CO emission from the clouds. We calculate the CO line emission from the GMCs utilizing an escape probability formalism. The radiation from these clouds then interacts with other clouds in the galaxy, and the level populations of CO are calculated by the balance of radiative absorptions, stimulated emission, spontaneous emission and collisions with H_2 and He.

At this point, the general reader should be equipped to understand the general results of this paper. For the remainder of this section, we elaborate on this abbreviated description. Throughout, we assume $h = 0.7$.

2.1 Smoothed particle hydrodynamic simulations of galaxies in evolution

We simulate the hydrodynamic evolution of both idealized isolated disc galaxies, and mergers between these discs. The purpose of the hydrodynamic simulations is to calculate the spatial distribution of the neutral ISM, stars and metals. It is from the neutral ISM that we will calculate the molecular gas properties, and, as we will discuss, the radiation from the stars and dust in the metals that determine the infrared (IR) radiation field. Here, we describe the components of the model most pertinent to this study, namely the physics of the ISM and star formation prescriptions. For a more full understanding of the underlying algorithms in GADGET-3, please refer to Springel & Hernquist (2002, 2003), Springel (2005) and Springel, Di Matteo & Hernquist (2005b).[3]

The galaxies are simulated with a modified version of the publicly available SPH code, GADGET-3 (Springel 2005). The ISM is modelled as two phase, with cold clouds embedded in a hot, pressure-confining medium (McKee & Ostriker 1977; Springel & Hernquist 2003). Numerically, this is realized via hybrid SPH particles. The cold gas mass grows via radiative cooling of the hot phase, and cold gas is converted to hot gas through the heating associated with star formation.

Stars form in the cold ISM according to a relation SFR $\propto \rho_{\rm cold}^{1.5}$. The normalization of this relation is set in order to match the local $\Sigma_{\rm SFR}$–$\Sigma_{\rm gas}$ relation (Kennicutt 1998a,b; Springel 2000; Cox et al. 2006b).

Supernova pressurization of the ISM is modelled via an 'effective' equation of state (EOS; see fig. 4 of Springel et al. 2005b). Here, we assume a modest pressurization of $q_{\rm EOS} = 0.25$ in the Springel et al. (2005b) formalism. This corresponds to a mass-weighted ISM temperature of $\sim 10^{4.5}$ K. In Appendix A we relax the star formation and EOS assumptions in order to test the validity of our results.

The simulations here are not cosmological: the discs are set up in an idealized manner in order to maximize spatial resolution. Here, the gravitational softening length for baryons is $100\,h^{-1}$ pc, and $200\,h^{-1}$ pc for dark matter. The discs are initialized according to the Mo, Mao & White (1998) formalism, and are bulgeless. They are embedded in dark matter haloes with Hernquist (1990) density distributions.

In order to compare with observations in a meaningful manner, we aim to simulate galaxies comparable to those found in the local Universe. Accordingly, our isolated discs are initialized inside haloes of mass $\sim 1.9 \times 10^{12}\,{\rm M}_\odot$, baryonic mass of $\sim 8 \times 10^{10}\,{\rm M}_\odot$, circular velocity of $160\,{\rm km\,s^{-1}}$ and with 40 per cent of the baryons in the form of gas.

The mergers are binary 1:1 mergers between discs constructed in the same manner. We simulate three mergers of slightly higher mass in order to ensure that they undergo a luminous starburst comparable to the most extreme ones seen in the local Universe ($\sim 100\,{\rm M}_\odot\,{\rm yr}^{-1}$). In particular, the discs that comprise the binary mergers have a rotation speed of $225\,{\rm km\,s^{-1}}$, halo mass of $\sim 5 \times 10^{12}\,{\rm M}_\odot$ and baryonic mass of $\sim 2.2 \times 10^{11}\,{\rm M}_\odot$. The mergers are set on an orbit with angles $(\theta_1, \phi_1, \theta_2, \phi_2) = (30, 60, -30, 45)$, $(-109, -30, 71, -30)$ and $(0, 0, 0, 0)$. The angles for the first two orbits are arbitrary, and were chosen to represent relatively 'normal' orbits in our library of simulations. The last merger is a coplanar one, and represents an extreme starburst with an extended duration, which we include simply for comparison. We choose the first merger as our 'fiducial' merger for the remainder of this paper as this particular model is well studied in the literature,[4] and focus particularly on the snapshot when the SFR is at its peak. The results from all simulations are similar, and we discuss the minor differences that do exist when necessary.

2.2 Physical properties of giant molecular clouds

We assume that the entire neutral mass in a given cell is locked in a cloud which is spherical, isothermal and of constant density. We determine the surface density of the neutral gas via

$$\Sigma_{\rm cloud} = \max(\Sigma_{\rm cell}, 100\,{\rm M}_\odot\,{\rm pc}^{-2}), \quad (3)$$

where $\Sigma_{\rm cell}$ is the surface density of the cell in the SPH simulation. In this model, when the cloud is resolved, we use the surface density as calculated in the simulations. When the cloud is unresolved, we

[3] We note that Springel et al. (2005b) describe the publicly available GADGET-2, whereas the work in this paper utilizes GADGET-3, a non-public modified version of GADGET-2. The main improvement in GADGET-3 over GADGET-2 is better load balancing on parallel processors.

[4] In Section 3, we discuss the physical and simulated observational properties of our fiducial merger to highlight its similarity to observed local galaxies.

adopt a subresolution surface density comparable to observed values of GMCs (e.g. Solomon et al. 1987; Blitz & Rosolowsky 2006).

We then determine the H_2 fraction of the neutral ISM utilizing the analytic formalism of Krumholz, McKee & Tumlinson (2008, 2009a) and McKee & Krumholz (2010). This prescription aims to model the balance between the dissociation of molecules by Lyman–Werner band photons, and the formation of molecules on dust grains. We refer the readers to the aforementioned papers for the full derivation, and simply repeat the numerical prescription here. The molecular fraction is given by

$$f_{\rm H_2} \approx 1 - \frac{3}{4}\frac{s}{1+0.25s} \quad (4)$$

for $s < 2$ and $f_{\rm H_2} = 0$ for $s \geq 2$. $s = \ln(1+0.6\chi+0.01\chi^2)/(0.6\tau_{\rm c})$, where $\chi = 0.76(1+3.1Z'^{0.365})$, and $\tau_{\rm c} = 0.066\Sigma_{\rm cloud}/({\rm M_\odot\ pc^{-2}})Z'$. Z' is the metallicity divided by the solar metallicity. This formalism for deriving $f_{\rm H_2}$ assumes chemical equilibrium.

It is worth a quick note that there are numerous prescriptions for determining the H I/H_2 balance in the ISM of simulations, some of which include time-dependent chemistry. Blitz & Rosolowsky (2006) developed an empirical pressure-based methodology for calculating the H_2 fraction in the neutral ISM, based on observations of local galaxies. Similarly, both semi-analytic models (Obreschkow et al. 2009; Obreschkow & Rawlings 2009), as well as full numerical solutions exist which model the effect of dissociating photons through models of galaxies (e.g. Pelupessy, Papadopoulos & van der Werf 2006; Dobbs et al. 2008; Robertson & Kravtsov 2008; Gnedin, Tassis & Kravtsov 2009; Pelupessy & Papadopoulos 2009; Gnedin & Kravtsov 2010). We motivate our usage of the analytic prescription of Krumholz et al. (2009a) for two reasons. First, some observational evidence suggests that on small scales (<100 pc), equation (4) may fare better than pressure-based prescriptions in describing the state of the neutral ISM in low-metallicity dwarf galaxies (Fumagalli, Krumholz & Hunt 2010). Secondly, a comparison between equation (4) and a numerical treatment of time-dependent chemical reaction network and radiative transfer in galaxies suggests that the analytic approximation is reasonable at metallicities above $0.01\,{\rm Z_\odot}$ (Krumholz & Gnedin 2011). Because we aim to model actively star-forming systems in this work, we find that the mass-weighted metallicity of our model clouds is always higher than this fiducial value and expect that the analytic approximation is therefore reasonable.

With $\Sigma_{\rm cloud}$ and $M_{\rm H_2}$ defined, the radius of the cloud is known. In order to account for the turbulent compression of gas, we scale the volumetric densities of the GMCs by a factor $e^{\sigma_\rho^2/2}$ where numerical simulations show

$$\sigma_\rho^2 \approx \ln\left(1+3M_{\rm 1D}^2/4\right), \quad (5)$$

where $M_{\rm 1D}$ is the one-dimensional (1D) Mach number[5] of the turbulence (Ostriker, Stone & Gammie 2001; Padoan & Nordlund 2002; see also Lemaster & Stone 2008). Because the temperature calculation is dependent on the density of the GMC (see below), solving for the density and temperature simultaneously is a computationally lengthy process for the multimillion-cell grids that concern us. Thus, to calculate the turbulence-driven density enhancement, we assume the temperature of the GMC is 10 K, which as we shall show, is a good approximation for the bulk of the GMCs in these simulations.

We calculate the 1D velocity dispersion in the cloud:

$$\sigma = \max(\sigma_{\rm cell}, \sigma_{\rm vir}), \quad (6)$$

where $\sigma_{\rm cell}$ is the mean square sum of the subgrid turbulent velocity dispersion within the GMC and the resolved non-thermal velocity dispersion. The subgrid turbulent velocity dispersion is calculated from the external pressure from the hot ISM (Robertson et al. 2004) using $\sigma^2 = P/\rho_{\rm cell}$ though we impose a ceiling of $10\,{\rm km\,s^{-1}}$ which comes from average values found in turbulent feedback simulations (e.g. Dib, Bell & Burkert 2006; Joung, Mac Low & Bryan 2009; Ostriker & Shetty 2011). The resolved non-thermal component is calculated by finding the turbulent velocity dispersion of the nearest neighbouring cells in the simulation. In detail, we calculate the standard deviation of the velocities of the nearest neighbour cells in the $\hat{x}$, $\hat{y}$ and $\hat{z}$ directions, and define the non-thermal velocity dispersion as the mean of these. In cases where the GMC is unresolved, a floor $\sigma_{\rm vir}$ is set by assuming the cloud is in virial balance with a virial parameter $\alpha_{\rm vir} = 1$, for $\alpha_{\rm vir} \equiv 5\sigma_{\rm vir}^2 R/(GM)$, so that

$$\sigma_{\rm vir} = 2.2\,{\rm km\,s^{-1}}\left[\frac{M}{10^5\,{\rm M_\odot}}\right]^{1/4} \quad (7)$$

for $\Sigma_{\rm cloud} = 100\,{\rm M_\odot\,pc^{-2}}$, where M is the mass of the cloud.

Finally, we calculate the temperature of the model GMCs. The model is based on that developed by Krumholz et al. (2011), and we describe the relevant details here as it is an important aspect of our model. The temperature of the molecular ISM is determined by a balance of heating and cooling processes in the gas, heating and cooling of the dust and a dust–gas thermal exchange. For the gas, we consider grain photoelectric heating at a rate per H nucleus $\Gamma_{\rm pe}$, cosmic ray heating at a rate $\Gamma_{\rm CR}$ and cooling via either C II or CO line cooling at a rate $\Lambda_{\rm line}$. The dust can be heated by the background infrared radiation field at a rate $\Gamma_{\rm dust}$, and cool via thermal emission at a rate $\Lambda_{\rm dust}$. Finally, there is an energy exchange between dust and gas at a rate $\Psi_{\rm gd}$, where $\Psi_{\rm gd}$ is positive if the dust is hotter than the gas. If the gas and dust are in thermal balance, then we have the following equations:

$$\Gamma_{\rm pe} + \Gamma_{\rm CR} - \Lambda_{\rm line} + \Psi_{\rm gd} = 0, \quad (8)$$

$$\Gamma_{\rm dust} - \Lambda_{\rm dust} - \Psi_{\rm gd} = 0. \quad (9)$$

The equation is solved by simultaneously iterating on the temperatures of the gas and dust.[6]

The grain photoelectric heating rate is assumed to be attenuated by half the mean extinction of the cloud (as the heating rate is expected to decrease toward the cloud interiors) and is given by

$$\Gamma_{\rm pe} = 4\times10^{-26} G_0'\, e^{-N_{\rm H}\sigma_{\rm d}/2}\,{\rm erg\,s^{-1}}, \quad (10)$$

where G_0' is the far-ultraviolet (FUV) intensity relative to the solar neighbourhood, and $\sigma_{\rm d}$ is the dust cross-section per H atom to UV photons. Here, we assume that the $G_0' = 1$ and $\sigma_{\rm d} = 1\times10^{-21}\,{\rm cm^{-2}}$. Test models in which we scale G_0 by the SFR density compared to that found in the solar neighbourhood (e.g. Ostriker, McKee & Leroy 2010) have similar results to those presented in this work, and are presented in Appendix A.

[5] We note that other authors have found a range of possible forms for equation (5). For example, Lemaster & Stone (2008) find $\sigma_\rho^2 \approx 0.6\ln(1 + 0.5M_{\rm 3D}{}^2)$, while Price, Federrath & Brunt (2011) find $\sigma_\rho^2 \approx \ln(1 + 1/9(M_{\rm 3D}{}^2))$, where $M_{\rm 3D}$ is the three-dimensional (3D) Mach number.

[6] We note that this dust temperature is not always the same as the temperature calculated by SUNRISE (Section 2.3). This makes little difference on the final results. We discuss this in more detail in Appendix A.

The cosmic ray heating rate is given by

$$\Gamma_{\rm CR} = \zeta' q_{\rm CR}\,{\rm s}^{-1}, \quad (11)$$

where ζ' is the cosmic ray ionization rate (here assumed to be $2 \times 10^{-17} Z'\,{\rm s}^{-1}$), and $q_{\rm CR}$ is the thermal energy increase per cosmic ray ionization. For H_2, $q_{\rm CR} \approx 12.25$ eV (though note that this value is quite uncertain; see discussion in appendix A4 of Krumholz et al. 2011), and for H I, $q_{\rm CR} = 6.5$ eV (Dalgarno & McCray 1972). We utilize a constant cosmic ray heating rate for all simulations. Some models suggest that there may be enhanced cosmic ray fluxes during starbursts which would increase the H_2 gas temperature (Papadopoulos 2010; Papadopoulos et al. 2010), and further enhance the effects found in our Results section.

Finally, in a subset of models we have explored the potential effects of turbulent heating on molecular clouds. In unresolved GMCs we can estimate this heating rate based on numerical experiments on the rate of turbulent dissipation: $\Gamma_{\rm turb} \approx 1.5 \times \sigma^3/R$, where R is the GMC radius (McKee & Ostriker 2007). For resolved GMCs, we can measure the turbulent heating rate directly from the code. Bulk turbulent motions can be converted to heat through two pathways: adiabatic compression and viscous dissipation. The compressive heating rate per unit mass is $\Gamma_{\rm comp} = P(\nabla \cdot \boldsymbol{v})/\rho$, and we can evaluate this directly from the density and velocity fields output by GADGET. The viscous dissipation rate per unit mass is $\Gamma_{\rm visc} = (\boldsymbol{\pi}_{\rm visc} \cdot \nabla) \cdot \boldsymbol{v}/\rho$, where $\boldsymbol{\pi}_{\rm visc}$ is the viscous stress tensor. The code relies on implicit dissipation rather than an explicit viscosity, but we can estimate the viscous heating rate produced by that implicit dissipation by noting that the Reynolds number must be $\sim$1 on the resolution scale of the code (Offner et al. 2009). This implies that the dynamic viscosity is $\eta \approx \rho v h$, where h is the SPH smoothing scale. Given this approximation, the components of the viscous stress tensor are $\pi_{ij,{\rm visc}} = \eta[\partial v_i/\partial x_j + \partial v_j/\partial x_i - (2/3)\partial v_i/\partial x_j \delta_{ij}]$, and which we can again evaluate directly from the density and velocity fields output by GADGET. We find that the effects of turbulent heating are modest in both the resolved and unresolved cases. In our fiducial merger including viscous dissipation reduces $X_{\rm CO}$ by $\sim$30 per cent, while the fiducial disc it reduces $X_{\rm CO}$ by less than a few per cent. Hereafter we neglect this heating term, though we note that including it would only enhance the results we present below.

The line cooling is assumed to occur via either C II or CO emission. The fraction of hydrogen for which the carbon is mostly in the form of CO is well approximated by the following result from both semi-analytic (Wolfire et al. 2010) and numerical (Glover & Mac Low 2011) work:

$$f_{\rm CO} = f_{\rm H_2}\, {\rm e}^{-4(0.53 - 0.045 \ln[G_0'/(n_{\rm H}/{\rm cm}^{-3})] - 0.097 \ln Z')/A_{\rm v}}. \quad (12)$$

When this fraction is above 50 per cent, we assume the cooling happens predominantly via CO line cooling; else, the cooling occurs via C II emission. The cooling rate is calculated via an escape probability formalism utilizing the public code of Krumholz & Thompson (2007). We describe the equations for the line radiative transfer (both within clouds, as is pertinent to calculating the cooling rates, and across the model galaxy, in Section 2.4).

The dust cooling rate is

$$\Lambda_{\rm dust} = \kappa(T_{\rm d}) \mu_{\rm H} c a T_{\rm d}^4. \quad (13)$$

We assume the bulk of the dust heating happens via IR radiation as IR radiation likely dominates the heating over UV flux in the optically thick centres of GMCs. The IR radiation field is known from SUNRISE dust radiative transfer calculations (which will be described in Section 2.3).

Finally, the dust and gas exchange energy via

$$\Psi_{\rm gd} = \alpha_{\rm gd} n_{\rm H} T_{\rm g}^{1/2} (T_{\rm d} - T_{\rm g}), \quad (14)$$

where the thermal gas–dust exchange rate is $\alpha_{\rm gd} = 3.2 \times 10^{-34} Z'\,{\rm erg\,cm^3\,K^{-3/2}}$ for H_2, and $\alpha_{\rm gd} = 1 \times 10^{-33} Z'\,{\rm erg\,cm^3\,K^{-3/2}}$ for H I (Goldsmith 2001).

2.3 Dust radiative transfer

In order to calculate the background radiation field from stars and the dust temperature, we perform dust radiative transfer calculations with the publicly available code SUNRISE. A full description of the algorithms can be found in Jonsson (2006), Jonsson, Groves & Cox (2010) and Jonsson & Primack (2010). Here, we summarize the aspects of the simulations most relevant to this study.

The sources of radiation in the model galaxies are stellar clusters and accreting black holes. The stellar clusters emit a template spectrum derived from STARBURST99 calculations, with the metallicities, masses and ages known from the GADGET-3 simulations. The active galactic nucleus (AGN) emits a spectrum based on observations of unreddened quasars (Hopkins, Richards & Hernquist 2007a), though has little effect in the calculations here (see Appendix A).

The substructure of the ISM on scales below the smoothing length of the SPH simulations is unresolved. We assume that star clusters with ages $<$10 Myr reside in natal birthclouds, and modulate their spectral energy distribution (SED) accordingly. These birthclouds contain H II regions and photodissociation regions (PDRs) whose SEDs are calculated utilizing 1D MAPPINGSIII photoionization models (Groves, Dopita & Sutherland 2004; Groves et al. 2008; Jonsson et al. 2010). The time-averaged PDR covering fraction is a free parameter. We assume a constant fraction of $f_{\rm PDR} = 0.3$, corresponding to a covering lifetime of $\sim$2–3 Myr (Groves et al. 2008). This value is motivated in part by simulations by Jonsson et al. (2010) which showed covering fractions comparable to these result in synthetic SEDs of disc galaxies comparable to the *Spitzer* Infrared Nearby Galaxies Survey (SINGS) sample (Kennicutt et al. 2003). Changing this parameter has minimal effects on the final results of this paper: we quantify this and other potential effects of the subresolution modelling in Appendix A.

When radiation leaves either the naked stellar cluster (with age $>$10 Myr), or the H II region/PDR (for younger clusters), it is allowed to interact with the diffuse ISM. We assume the remaining cold molecular phase has an negligible cross-section for interaction, though test the effects of this assumption in Appendix A.

The dust mass in the diffuse ISM is calculated assuming a constant dust to metals ratio of 0.4 (Dwek 1998; Vladilo 1998; Calura, Pipino & Matteucci 2008), where the metallicity distribution is known from the SPH calculations. We use the Weingartner & Draine (2001) dust model with $R \equiv A_V/E(B-V) = 3.15$, as updated by Draine & Li (2007). The dust and radiation field are assumed to be in radiative equilibrium, utilizing the methodology of Juvela (2005) for calculating the converged radiation field. When the radiation field has converged, we calculate the dust temperature in each cell by iterating equations (6)–(8) of Jonsson & Primack (2010) utilizing a Newton–Raphson scheme.

2.4 Molecular line radiative transfer

Finally, with information about the spatial distribution of GMCs in the model galaxies, and their mean H_2 fractions, densities, temperatures, velocity dispersions and kinematics through the galaxy, we are prepared to calculate the emergent CO line emission from

the model galaxy. This involves two stages. First, we calculate the escape probabilities of the CO lines from the GMCs. We then track the propagation of these photons through the model galaxy as they potentially interact with other GMCs.

Generally, CO line emission is set by the level populations. The source function from a given region for a given transition from upper level to lower level $u \rightarrow l$ is given by

$$S_\nu = \frac{n_u A_{ul}}{(n_l B_{lu} - n_u B_{ul})}, \tag{15}$$

where A_{ul}, B_{lu} and B_{ul} are the Einstein coefficients for spontaneous emission, absorption and stimulated emission, respectively, and n is the absolute level populations.

We first calculate the level populations within and probability for photons to escape from the individual GMCs in the galaxy utilizing the publicly available code described in Krumholz & Thompson (2007). The levels are assumed to be in statistical equilibrium and determined through the rate equations:

$$\sum_l (C_{lu} + \beta_{lu} A_{lu}) f_l = \left[\sum_u (C_{ul} + \beta_{ul} A_{ul}) \right] f_u, \tag{16}$$

$$\sum_i f_i = 1, \tag{17}$$

where C are the collisional rates, f the fractional level populations and β_{ul} is the escape probability for transition $u \rightarrow l$. The rate equations can be rearranged as an eigenvalue problem, and solved accordingly.

The escape probability, β_{ul}, can be approximated by relating it to the optical depth in the line, τ_{ul} (Krumholz & Thompson 2007):

$$\beta_{ul} \approx \frac{1}{1 + 0.5\tau_{ul}}. \tag{18}$$

In the escape probability formalism, the optical depth of the line through the cloud can be represented as

$$\tau_{ul} = \frac{g_u}{g_l} \frac{3 A_{ul} \lambda_{ul}^3}{16(2\pi)^{3/2}\sigma} Q N_{\rm H_2} f_l \left(1 - \frac{f_u g_l}{f_l g_u} \right), \tag{19}$$

where Q is the abundance of CO with respect to H_2, g_l and g_u are the statistical weights of the levels, $N_{\rm H_2}$ is the column density of H_2 through the cloud, λ_{ul} is the wavelength of the transition and σ is the velocity dispersion in the cloud. Equations (16)–(19) are iterated upon utilizing the Newton–Raphson method until the escape probabilities and level populations within the GMCs are known.

With β_{ul} calculated, we determine the effects of radiation from individual GMCs on other GMCs in determining the final level populations utilizing the 3D non-local thermodynamic equilibrium (LTE) Monte Carlo radiative transfer code TURTLEBEACH (Narayanan et al. 2006b, 2008b). We begin with the level populations found from the escape probability calculations as a guess, and emit model photons from each GMC isotropically with direction drawn randomly, and emission frequency drawn from a Gaussian profile function:

$$\phi(\nu) = \frac{1}{\Delta\nu_{\rm D}\sqrt{\pi}} \exp\left\{ -\left(\nu - \nu_0 - \boldsymbol{v} \cdot \hat{\boldsymbol{n}} \frac{\nu_{ul}}{c} \right)^2 / \Delta\nu_{\rm D}^2 \right\}, \tag{20}$$

where ν_0 is the rest frequency of the line, $\boldsymbol{v}$ is the velocity of the cloud in the direction of the photon's emission, c is the speed of light and $\Delta\nu_{\rm D}$ is the Doppler width of the emission line.

When the photon passes through a cell, it interacts with a GMC and sees an opacity of

$$\alpha_\nu^{ul}({\rm gas}) = V_{\rm fill} \left[\frac{h\nu_{ul}}{4\pi} \phi(\nu)(n_l B_{lu} - n_u B_{ul}) \right], \tag{21}$$

where $V_{\rm fill}$ is the volume filling factor of the spherical GMC. We neglect absorption by dust in this model.

After all GMCs have emitted some number of model photons, the level populations in the GMCs are updated by assuming detailed balance:

$$n_l \left[\sum_{k<l} \beta_{lk} A_{lk} + \sum_{k \neq l} (B_{lk} J_\nu + C_{lk}) \right] = \sum_{k>l} n_k \beta_{kl} A_{kl} + \sum_{k \neq l} n_k (B_{kl} J_\nu + C_{kl}), \tag{22}$$

where C_{lk} and C_{kl} are the collisional rates, and β only exists for transition $k \rightarrow l$ such that $k = l + 1$. Equation (22) is solved via Gauss–Jordan matrix inversion.

This process is iterated upon until the level populations have achieved convergence. Here, we demand that they not vary by more than a fractional difference of 1×10^{-3} for at least three iterations.

Once the level populations have been solved for, we build the formal spectrum by choosing an (arbitrary) viewing angle, and integrating along lines of sight (e.g. Walker, Narayanan & Boss 1994):

$$I_\nu = \sum_{z_0}^{z} S_\nu(z) \left[1 - {\rm e}^{-\tau_\nu(z)} \right] {\rm e}^{-\tau_\nu({\rm tot})}. \tag{23}$$

Tests of TURTLEBEACH against the publicly available Leiden benchmarks (van Zadelhoff et al. 2002) are presented in Narayanan et al. (2006b). We obtained our coefficients from the Leiden Atomic and Molecular Database (Schöier et al. 2005). We assume a fractional carbon abundance of 1.5×10^{-4}, though the abundance of CO with respect to H_2 is given by equation (12).

3 OBSERVATIONAL AND PHYSICAL PROPERTIES OF SIMULATED GALAXIES

As we aim to compare potential variations in $X_{\rm CO}$ in our simulated galaxy mergers to those that are actually observed, it is worth briefly comparing the physical and synthetic observational properties of our model galaxies to real galaxies. Our fiducial merger has been well studied in the literature, and is very much an average merger simulation as far as the range of simulated SFRs, black hole accretion rates and bolometric luminosities. While the processes described in this section generically describe gas-rich mergers, what we summarize here has been calculated and published previously explicitly for our fiducial model.

The merger goes through elevated SFR upon first passage as tidal torques on the gas cause the gas to lose angular momentum and fall toward the centres causing high-density regions (Mihos & Hernquist 1996; Hopkins et al. 2006; Narayanan et al. 2008c; Juneau et al. 2009). The galaxy undergoes a starburst upon final coalescence, and peaks in its bolometric luminosity. Radiative transfer post-processing on these models has found that the model galaxy is then visible as a ULIRG (Chakrabarti et al. 2007). The same gaseous inflows can drive sufficient black hole growth to result in optical quasar activity (Di Matteo, Springel & Hernquist 2005; Hopkins et al. 2005a,b, 2006). Effects of the AGN feedback can be seen in both the warm infrared colours of the galaxy (Younger et al. 2009), as well as molecular outflows (Narayanan et al. 2006a, 2008b).

The truncation of the starburst by a combination of gas consumption and AGN feedback can render the galaxy observable as an E+A post-starburst (Snyder et al. 2011) before it evolves into a dead early type (Springel, Di Matteo & Hernquist 2005a; Hopkins et al. 2007b) with colours comparable to those observed on the red sequence (Springel et al. 2005a; Hopkins

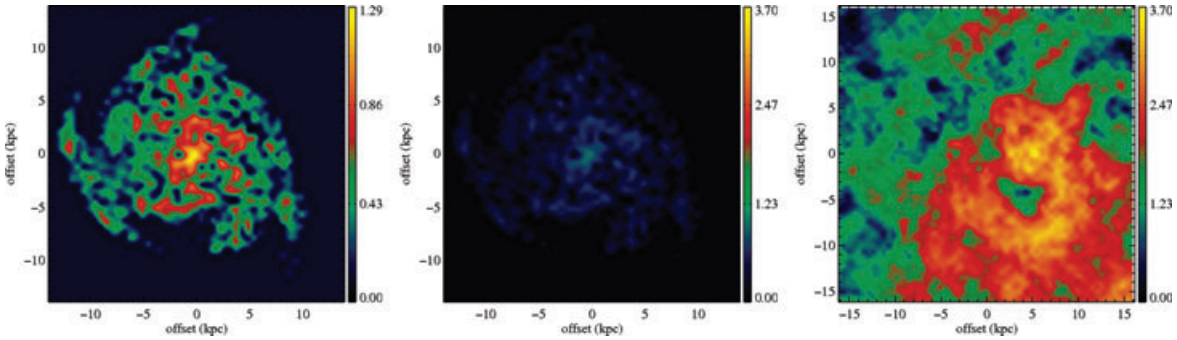

Figure 1. Velocity-integrated brightness temperature W_{CO} maps for model disc galaxy (left), and fiducial merger snapshot (right). The colour scales correspond to the colour bars on the right of each panel, and the units are $\log_{10}$ (K km s^{-1}). The centre panel shows the model disc again, but with the same colour scale as the merger for comparison. Low gas kinetic temperature ($\sim$10 K) and velocity dispersions cause the bulk of the disc galaxy to have intensities of $\sim$10 K km s^{-1}. In contrast, the velocity dispersion within GMCs in the ULIRG can be many tens of km s^{-1}, with gas kinetic temperatures near 50 K. Summed over a sightline, the observed gas intensity can be $>10^3$ K km s^{-1}.

et al. 2008b,c). The kinematic (Cox et al. 2006c), X-ray (Cox et al. 2006a), nuclear emission (Hopkins et al. 2008a, 2009) and molecular disc properties (Xu, Narayanan & Walker 2010) of this merger remnant have all been studied and found to be comparable to those observed. Similarly, the remnant lies on the Fundamental Plane (Di Matteo, Springel & Hernquist 2005; Robertson et al. 2006; Hopkins, Cox & Hernquist 2008d).

4 RESULTS

4.1 GMCs in 'normal' discs

In the far left-hand panel of Fig. 1, we show the velocity-integrated brightness temperature map of the model disc galaxy. As expected, the central regions are the brightest, and the outer disc has little CO emission. In the top left-hand panel of Fig. 2, we plot the emission-weighted distribution of X_{CO} values for the GMCs in our model disc galaxy and the fiducial model merger. We additionally plot the distribution of GMC physical properties in both the disc and merger. We will return to this plot frequently throughout this section and the next.

The luminosity-weighted X_{CO} in our model disc is $\sim 4 \times 10^{20}$ cm^{-2}/K km s^{-1} with a relatively narrow dispersion. The dispersion is narrow because the surface densities, kinetic temperatures and velocity dispersions of the model disc GMCs show fairly little variation. To remind the reader, the column densities in the GMCs in our disc galaxy are set to be the surface density of cold gas in the cell. When the GMC is unresolved in the simulation, we set the subgrid value of the surface density to $\Sigma_{cloud} = 100\,M_\odot$ pc^{-2}. This value was chosen to match the roughly constant surface density of Galactic molecular clouds. Nearly all of the GMCs in the model disc take on this value for a surface density.

The kinetic temperatures of GMCs in the disc have a relatively tight distribution near 10 K, as shown in Fig. 2. Because the GMCs have a relatively low density compared with starbursts (the mass-weighted value is $\sim$500 cm^{-3}), there is little coupling with the dust grains (which are a factor of a few hotter; Fig. 2). Thus the temperature is primarily determined by molecular line cooling, and heating by cosmic rays and the grain photoelectric effect. The kinetic temperature helps to set the brightness temperature, though the two are not identical. The emission-weighted brightness temperature for the merger(disc) is $\sim$50(7) K.

Finally, the distribution of velocity dispersions in the GMCs is fairly narrow. Recalling Section 2, the velocity dispersion of the clouds is taken by calculating the dispersion amongst the cell's nearest neighbours, with a subgrid model for unresolved clouds (equation 7). Because the disc is dynamically cold, the velocity dispersions are primarily set by the latter case. This results in an emission-weighted velocity dispersion within GMCs in the model disc of $\sim$3 km s^{-1}, with a maximum of $\sim$15 km s^{-1}. These values compare favourably with the velocity dispersions reported in the comprehensive survey of Solomon et al. (1987), and the more recent review by Blitz et al. (2007).

We can ask why the simulated X_{CO} from the model galaxy is comparable to the Galactic average, $X_{CO} \approx 2$–4×10^{20} cm^{-2}/K km s^{-1}. In principle this occurs because the physical conditions in the model GMCs by and large match those of observed GMCs in the Milky Way. In this sense, the fact that our model value for X_{CO} in quiescent discs matches that of the Galaxy is by construction. However, there are two salient points here.

First, it is important to remember that we allow for the possibility that the galactic environment can set the physical conditions in the GMCs if the pressure is sufficiently high. The fact that the default value for the surface density and velocity dispersions in the clouds is typically used is a statement that the galactic environment in the model disc galaxy is not sufficiently extreme to cause significant changes in the surface densities, temperatures or velocity dispersions in the GMCs from the Galactic values. As we will see in the subsequent section, this is not the case in mergers.

Secondly, the subresolution values for the GMCs are not without physics. GMCs through the Local Group are observed to obey the Larson (1981) relations: they follow a linewidth–size relationship with $\sigma \propto R^{0.5}$, they have virial parameters $\alpha \sim 1$ and they all have roughly the same surface density $\Sigma \sim 100\,M_\odot$ pc^{-2} (Blitz et al. 2007; Bolatto et al. 2008). The origin of these observed relationships is debated, but their universality argues for some sort of internal regulation mechanism operating in GMCs (e.g. Krumholz, Matzner & McKee 2006; Shetty & Ostriker 2008). Regardless of the underlying mechanism, though, our subgrid model is not simply tuned to reproduce the 'right' X_{CO}. Instead, it models the real physical properties of GMCs.[7]

[7] We note, however, that clouds need not be virialized to have X_{CO} comparable to observed galactic values. Provided that Σ_{cloud}, T and σ remain within a modest range of values, $X_{CO} \sim 2$–4×10^{20} cm^{-2}/K km s^{-1} (Shetty et al. 2011b).

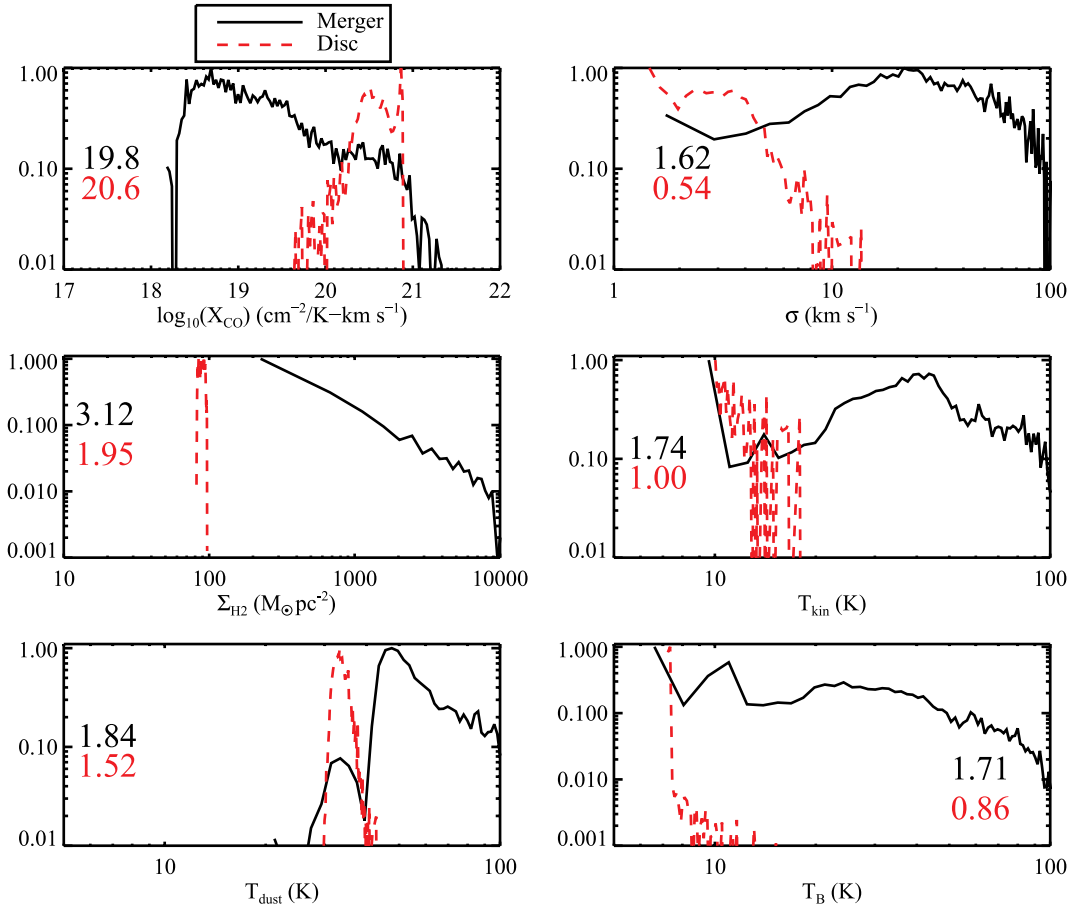

Figure 2. Emission-weighted distributions of X_{CO} values and physical properties for the GMCs in the model disc galaxy (red dashed line) and fiducial merger model (solid black line). The ordinate values are normalized. Starting from the top left, and going clockwise, the plots show X_{CO}, velocity dispersion, kinetic temperature, brightness temperature, dust temperature and GMC surface density. The disc galaxy predominantly has GMCs with physical properties comparable to the Milky Way's, and thus has similar X_{CO} values. The GMCs in the merger show a broad distribution in X_{CO} values, with a lower mean than the disc galaxy. The lower X_{CO} owes to larger gas temperatures (which are larger due to efficient coupling with the warm dust at high densities) and large velocity dispersions in the gas. The numbers in each panel refer to the $\log_{10}$ of the emission-weighted mean value, and the black (top) number corresponds to the merger whilst the red (bottom) corresponds to the disc. Because the numbers correspond to the $\log_{10}$ of the mean in the physical quantities, they will have larger values than one would pick by eye in the log–log plots.

Finally, it is important to note that the results presented in this section do not necessarily translate to disc galaxies at high redshift. Galaxies on the 'main sequence' of SFRs at high z (e.g. Noeske et al. 2007a,b) still form stars at rates comparable to present-epoch mergers (Daddi et al. 2005, 2007) because they have very high gaseous surface densities, though they may be morphologically classified as discs (Förster Schreiber et al. 2009).

4.2 X_{CO} in merger-driven starbursts

We now turn to X_{CO} in galaxy mergers. Before embarking on the remainder of this section, it is important to emphasize that the many of the GMCs in the model starburst are resolved (this is clear from the Σ_{H_2} panel in Fig. 2). Thus, the derived values for X_{CO} are independent of subresolution assumptions.

During the merger, gas is funnelled toward the nuclear regions, causing dense concentrations of molecular gas (Barnes & Hernquist 1991, 1996). The surface densities of the GMCs in our simulations rise accordingly. In principle, this would cause a rise in the CO–H_2 conversion factor (cf. equation 2). However, during the merger-induced starburst, the increase in velocity-integrated line intensity exceeds the rise in surface density, causing X_{CO} to drop from the Galactic value.

In Fig. 3, we show the evolution of the SFR, gas temperature, velocity dispersion and X_{CO} as a function of time for the three model galaxy mergers. The shaded region denotes the range of mean values among the GMCs within the merger models at each time-step, i.e. at time 0 the lowest point outlined in grey corresponds to the lowest galaxy-averaged value of the three merger models, and the highest point in grey corresponds to the highest galaxy-averaged value among the three. The time axes are centred around the peak in the starburst for each model. When the galaxies merge, the discs are destroyed. During this time, the dominant contributor to σ within the GMCs is the non-thermal component derived from the local resolved velocity dispersion of the gas. The non-thermal velocity dispersion is driven by the dynamics during the galaxy merger and mixing of stellar mass with the H_2 gas.

During final coalescence in the merger, when the SFR peaks at a few hundred $M_\odot\ yr^{-1}$, the fraction of dense gas rises, a result verified both in theoretical models (e.g. Mihos & Hernquist 1994, 1996; Narayanan, Cox & Hernquist 2008a; Narayanan et al. 2008c; Bournaud et al. 2011), and observations (Juneau et al. 2009). The

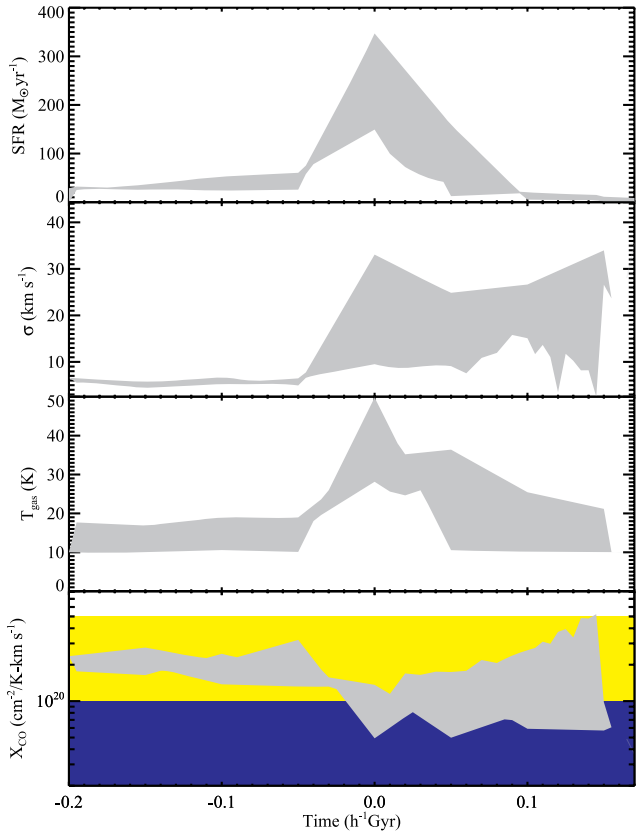

Figure 3. The evolution of the SFR, emission-weighted velocity dispersion, kinetic temperature and X_{CO} of the individual GMCs within the galaxies for all three merger models as a function of time. The time axes are centred for each model about the point of maximum SFR. The grey shaded region denotes the range in emission-weighted mean values for all three models. This means that at a given time-step, the shaded region is defined by the maximum and minimum value of a given quantity seen among the three merger models. In the bottom panel, the yellow and blue bands denote the typical ranges of X_{CO} observed for the Galaxy and ULIRGs, respectively (as compiled by Tacconi et al. 2008). Prior to the burst, the inspiralling discs have X_{CO} values comparable to the Galactic mean. Upon the merger, increased velocity dispersions and gas temperatures contribute to lowering X_{CO}. In the post-merger stage, differences in H_2 abundances, CO abundances and time for the gas to revirialize contribute toward a large dispersion in X_{CO} values.

mass-weighted mean GMC density rises to roughly $\gtrsim 10^4\,cm^{-3}$, compared to $\sim$500 cm^{-3} in the model disc. At these high densities, the energy exchange between dust and gas becomes efficient, and the gas temperatures begin to approach the dust temperatures. At the same time, the dust is being heated by an amplified radiation field due to the merger-induced starburst. This is demonstrated explicitly in Fig. 2, where we show the dust and gas (kinetic) temperature distributions of the GMCs in the model galaxies. The mean gas temperature is higher by a factor of a few than the roughly $\sim$10 K GMCs in the model disc. The rise in the gas kinetic temperature during the starburst is shown in Fig. 3 as well.[8]

[8] We remind the reader that we adopt a constant cosmic ray ionization rate in all models. If cosmic ray energy densities increase in starburst environments as suggested by recent observational (Abdo et al. 2010a) and theoretical (Papadopoulos 2010; Papadopoulos et al. 2010) work, then the gas temperatures would further increase, causing X_{CO} in starbursts to fall even further (though see Bell et al. 2006, for an expanded study on the role of cosmic rays in the *X*-factor at various extinctions).

The large molecular gas densities in the merger also mean the CO is thermalized in the ground state transition. When level populations are in LTE, their source function can be described by the Planck function. In this limit, the source function rises with temperature. Hence, the rise in gas kinetic temperature during the burst contributes to driving X_{CO} down.

The combination of the increased velocity dispersion and the brightness temperature combine to exceed the increase in surface density, which causes a depressed mean X_{CO} from the Galactic value during the merger. We now return to the first panel of Fig. 2 to explicitly compare X_{CO} in the merger against the disc galaxy. We see that X_{CO} has a broad distribution for the model merger. A number of GMCs outside of the nucleus are similar to the disc galaxy's in terms of their physical properties. These GMCs are unresolved in our simulations (owing to the fact that they reside in lower density environments), and thus take on surface density and velocity dispersion values comparable to those observed in the Galaxy. However, the GMCs toward the centre of the galaxy all have larger surface densities, velocity dispersions and kinetic temperatures. The latter two combine to depress X_{CO} compared to the values seen in the disc by a factor of $\sim$5–10. Because most of the mass in the merger is in the central regions, the luminosity-weighted mean is low. Test simulations with fixed temperatures or velocity dispersions show that the increased kinetic temperature and velocity dispersion in the gas contribute roughly equally to the increased line intensity in the merger simulation. This is somewhat apparent from Fig. 2, where we see similar distributions values for the kinetic temperatures and velocity dispersions in the gas.

The magnitude by which X_{CO} decreases is dependent on the strength of the merger. Turning to Fig. 3, we see a range in X_{CO} values during the burst. The model with the largest X_{CO} during the burst corresponds to the lowest peak SFR. A key point of this aspect of the model is that there is no 'merger value' of X_{CO}: X_{CO} depends on the physical parameters of the emitting galaxy.

What happens in the post-starburst stage is also highly merger specific. During this phase, the galaxy is a gas-poor early type. Generally, the gas has a large velocity dispersion for at least a dynamical time after the burst. This is consistent with what was seen in simulations of CO gas in high-*z* submillimetre galaxies (Narayanan et al. 2009). During this phase, it is less trivial to simply relate the observed X_{CO} to the gas velocity dispersion and temperature as there is a much larger dispersion in molecular gas fractions and CO abundances. This owes to the fact that there are highly varying physical conditions in the post-burst galaxy, which drive strong variations in the H_2 and CO abundances. Some of the simulations return to a Galactic X_{CO} value quickly, while others remain low.

In summary, during the merger-induced starburst, X_{CO} drops in galaxies from the standard Galactic value due to increased gas temperatures and velocity dispersions. During this time, the CO abundances are $\sim 1 \times 10^{-4}/H_2$ and molecular gas fractions near unity in the main CO emitting region. In the resulting gas-poor merger remnant, the dynamical and thermal history can vary from model to model, and the evolution of X_{CO} is less uniform among mergers.

4.3 The variation of X_{CO} with galactocentric radius

With the concepts presented in Section 4.2, we are now in a position to understand how X_{CO} varies in galaxies as a function of spatial location. In Fig. 4, we show the simulated X_{CO} maps for the disc galaxy and fiducial merger, and in Fig. 5, we plot the values for X_{CO} in the GMCs in our model disc galaxy and fiducial merger

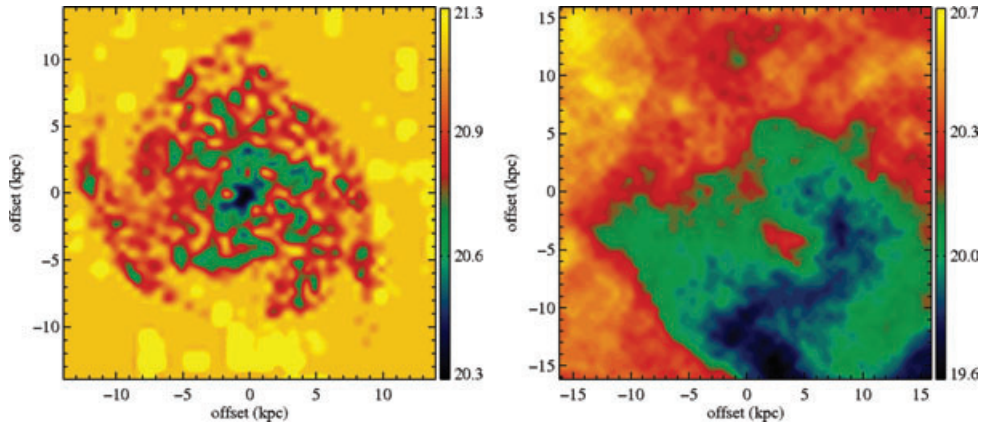

Figure 4. Maps of X_{CO} for the fiducial disc galaxy and merger. The colour scale denotes $\log_{10}$ (cm^{-2}/K km s^{-1}). X_{CO} is lower toward the centre of the disc galaxy due to higher temperatures and velocity dispersions in the clouds. The warm and high-σ gas is somewhat more spread out in the merger. We enforce a maximum X_{CO} in the colour bar of the disc galaxy of 21.3 to aid in clarity, though there are a few pixels with values as high as 21.8.

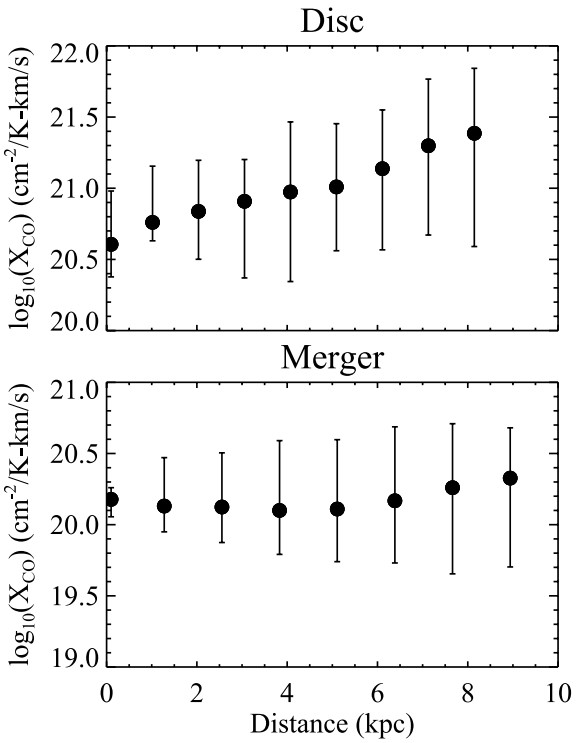

Figure 5. X_{CO} as a function of spatial distribution for the molecular gas in model disc (top) and merger (bottom). The X_{CO} is derived from the maps (Fig. 4), and is the emission-weighted mean X_{CO} in bins of galactocentric distance. The bars around the points represent the range of X_{CO} values within a given distance bin. The molecular gas at the centre of the disc has systematically lower X_{CO} values than the outer disc. In the merger, X_{CO} shows a wide range of values throughout the galaxy.

as a function of radius from the centre of the galaxy. The X_{CO} values from Fig. 5 come from the map in Fig. 4. The X_{CO} values are binned in bins of distance, and represent the emission-weighted mean within a given distance bin. The bars denote the range of X_{CO} values seen in a given distance bin.

X_{CO} in the centre of the model disc galaxy is systematically lower than in the rest of the galaxy. In particular, a number of GMCs along the line of sight have velocity dispersions larger than the typical virialized values, with values elevated by a factor of ∼2. Similarly, due to the elevated densities in the nucleus combined with a warmer dust temperature, the gas temperatures of some GMCs can reach values up to 15 K. This causes X_{CO} in the central kiloparsec to generally display the lowest values in the galaxy. Depressed values of X_{CO} from the Galactic mean have been observed in at least a few GMCs toward the Galactic Centre (Oka et al. 1998). It is important to note that the regions where $X_{CO} > 10^{21}$ cm^{-2}/K km s^{-1} represents much of the area, but a negligible fraction of the gas mass in the galaxy. This is evident from Fig. 2.

In the fiducial model merger, unlike the situation with the model disc galaxy, we see no clear trend in X_{CO} with galactocentric radius. Because of the violent nature of the gas dynamics during the merger, gas of a variety of physical conditions is mixed together. Consequently, we see a large range of X-factors in the GMCs throughout the galaxy.

Because the emission from the merger is irregular, it is possible that by choosing a different centre, the results from Fig. 5 would change. To test this, we recentred the image on the peak of the velocity-integrated intensity. Doing this provides no substantial change in the results of Fig. 5.

5 DISCUSSION

5.1 Observational consequences of the model

We have presented a model in which X_{CO} in GMCs is dependent on the physical conditions within the clouds. When the surface densities, kinetic temperatures and velocity dispersions within the GMCs resemble those of observed clouds in the Galaxy, the resulting X_{CO} factor is comparable to the observed Galactic mean value. In starbursts, while the surface densities of clouds are higher, this is offset by both larger velocity dispersions in the GMCs as well as larger gas temperatures. The increased linewidths represent the turbulent velocity dispersion in the merger, as well as the stellar potential. The increased gas temperatures owe to efficient coupling with the dust at the high densities encountered in a merger. A fundamental point of this study is that the physical conditions which cause X_{CO} to vary in starbursts are coupled. The same processes which drive the increased gas surface density also cause an increase in SFR which drives up the dust and consequently the gas temperatures. Similarly, in a merger-driven burst, the gas velocity dispersion rises during the merger.

While it is of utmost importance to parametrize $X_{\rm CO}$ in terms of observable properties, because the physical parameters which drive observed values of $X_{\rm CO}$ are coupled, this is a non-trivial task which is outside the scope of this work (though it will be investigated in a forthcoming paper). Empirically, there is a tentative trend that $X_{\rm CO}$ decreases with increasing galaxy surface density (Tacconi et al. 2008). In the context of the models presented here, such a trend is plausible (see also Shetty et al. 2011b). One might expect that higher surface density systems typically arise in situations when the velocity dispersion is high and the SFRs, dust temperatures and gas temperatures are also high.

While the models investigated here by no means comprise an exhaustive parameter-space study of galaxy masses, merger mass ratios or merger orbits, we can investigate whether $X_{\rm CO}$ can be parametrized by $\Sigma_{\rm H_2}$ in the simulations. To increase the dynamic range of surface densities in our models, we include one additional simulation of a high-redshift merger. The merger is the model submillimetre galaxy of Hayward et al. (2011) during the coalescence when the peak merger-induced starburst is $\sim$4500 $\rm M_\odot\,yr^{-1}$. The model submillimetre galaxy has been shown to reproduce both the observed SED (Narayanan et al. 2010a), CO properties (Narayanan et al. 2009), overlap with 24 μm sources (Narayanan et al. 2010b) and number counts of observed submillimetre galaxies (SMGs; Hayward et al. 2010). Similarly, to increase the number of galaxies in our sample, we include many snapshots for the mergers (i.e. not just the snapshots at peak SFR).

We plot the emission-weighted mean $X_{\rm CO}$ of the GMCs in our model galaxies versus their emission-weighted mean surface densities in Fig. 6. The models include the model mergers described in Section 2, the model disc galaxy and the newly introduced model submillimetre galaxy. The galaxies are binned by $\Sigma_{\rm H_2}$. The trend seen is what is expected: that $X_{\rm CO}$ should decrease with gas surface density. In principle this owes to the fact that the highest surface density galaxies in our simulations are also forming stars at 10^2–10^3 $\rm M_\odot\,yr^{-1}$, and have relatively large velocity dispersions. However, we emphasize strongly that Fig. 6 is to be taken as a qualitative trend, rather than robust. A larger parameter-space survey of the simulations will be undertaken for a future study to identify the true mean and dispersions of $X_{\rm CO}$ as a function of $\Sigma_{\rm H_2}$.

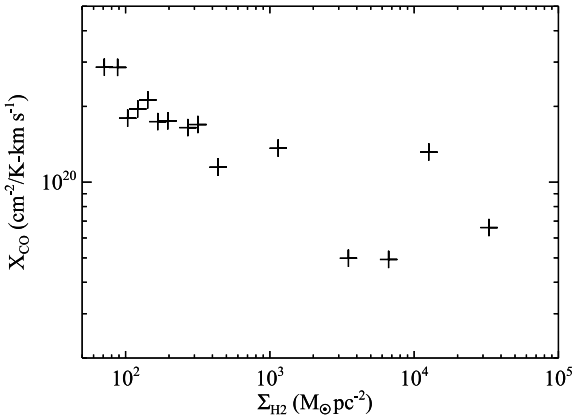

Figure 6. Emission-weighted mean $X_{\rm CO}$ in GMCs for each model galaxy versus their emission-weighted mean surface density. The points represent the mean values for all of the GMCs within individual galaxies, and the galaxies are binned by surface density. In order to increase our sample size, many snapshots (i.e. not just the peak SFR for the mergers), as well as a model submillimetre galaxy, were included in this plot. Higher surface density environments tend to correspond with merger-driven starbursts in our models, and hence larger values of σ and $T_{\rm K}$. In these cases, $X_{\rm CO}$ tends to be lower than the standard Galactic value.

The variation in $X_{\rm CO}$ with environment may have implications for observed KS star formation laws. An example of this was presented by Daddi et al. (2010) and Genzel et al. (2010) who applied a starburst $X_{\rm CO}$ value to the inferred mergers in their observed sample of galaxies, and a Galactic $X_{\rm CO}$ value to the discs. Doing so results in a bimodal SFR surface density–gas surface density relation. On the other hand, Ostriker & Shetty (2011) pointed out that if a simple Σ-dependent $X_{\rm CO} \propto \Sigma^{-0.5}$ is used above $\Sigma_{\rm H_2} = 100\,\rm M_\odot\,pc^{-2}$, a unimodal empirical star formation relation results (with $\Sigma_{\rm SFR} \propto \Sigma^2$, consistent with theoretical expectations for self-regulated star formation in this regime).

Interpreting results for high-redshift galaxies in the context of our model are complex. Our model advocates for lower $X_{\rm CO}$ values in high surface density environments. However, galaxies at $z \sim 2$ which have surface densities comparable to local ULIRGs may in fact be discs (e.g. Daddi et al. 2005; Genzel et al. 2006; Förster Schreiber et al. 2009; Hopkins et al. 2010). How $X_{\rm CO}$ of high-z discs should scale in this model is unclear at present. While their surface densities are comparable to local ULIRGs, their velocity dispersions may not show the same enhancement as seen in our model mergers. However, their gas temperatures may be comparable to their dust temperatures if the densities are high enough. Work by the Chicago group (Feldmann et al., in preparation) is underway to investigate this. Either way, the fact that our results tentatively suggest a relationship between $X_{\rm CO}$ and surface density implies a continuum in $X_{\rm CO}$ values, rather than a bimodality. Thus the relationship between our model results and the interpretation of high-z observations by Daddi et al. (2010) and Genzel et al. (2010) will depend on the distribution of surface densities in their observed galaxies, among other issues. We note, however, that our work, like that of Teyssier, Chapon & Bournaud (2010), is consistent with the idea that the observed behaviour in the SFRs and $X_{\rm CO}$ can be explained without the need to invoke a volumetric star formation law that is different in discs and mergers. The change in $X_{\rm CO}$ we see in our simulations occurs because of changes in the physical conditions of GMCs associated with the merger, and not because the underlying star formation law is different.

Finally, the concepts presented in this paper are testable in the near future with ALMA. Our models suggest that high spatial resolution observations of nearby ULIRGs will display both large velocity dispersions in the CO gas, and larger brightness temperatures than those seen in observations of Galactic GMCs on a comparable scale. We see this when comparing the panels of Fig. 1. Some observational evidence for this already exists. Interferometric surveys of the central regions of nearby ULIRGs show velocity dispersions of hundreds of $\rm km\,s^{-1}$, and brightness temperatures of tens of Kelvin (e.g. Scoville, Yun & Bryant 1997; Downes & Solomon 1998). Similarly, unresolved observations of starbursts have shown gas and dust temperatures in the range of 30–50 K, in agreement with the models presented here (Yao et al. 2003; Narayanan et al. 2005; Leech et al. 2010; Mao et al. 2010; Mühle et al. 2011).

5.2 Relationship to other models

The seminal work of Maloney & Black (1988) investigated $X_{\rm CO}$ in galaxies via subresolution models of GMCs in a disc-like configuration. These authors found that $X_{\rm CO}$ would vary from the Galactic value in cases of high kinetic temperature, high velocity dispersion or low metallicity. While not simultaneously modelling any

of these effects, this model identified some of the most important driving factors in setting the observed X-factor in clouds.

A number of other studies have also investigated $X_{\rm CO}$ in models of GMCs. Early studies implemented 1D radiative transfer calculations in spherical models of GMCs (e.g. Kutner & Leung 1985; Wall 2007). With the increase of computational power, 3D numerical studies of GMCs in evolution have recently become feasible. Recently, Glover et al. (2010) and Glover & Mac Low (2011) modelled H_2 and CO formation/destruction in MHD models of GMCs. These models were elaborated upon by Shetty et al. (2011a,b) who utilized radiative transfer calculations in combination with these MHD models to produce bona fide observables from the model clouds. These authors found that model GMC with mean densities, column densities, temperatures and velocity dispersions comparable to the Milky Way's clouds ($n \sim 10^2$–$10^3\,{\rm cm^{-3}}$, $N_{\rm H_2} \sim 10^{21}$–$10^{22}\,{\rm cm^{-2}}$, $T \sim 10$–$20\,{\rm K}$, $\sigma \sim 1$–$6\,{\rm km\,s^{-1}}$) had average $X_{\rm CO}$ factors of order 2–$4 \times 10^{20}\,{\rm cm^{-2}/K\,km\,s^{-1}}$, and were insensitive to detailed temperature and velocity distributions. When manually increasing the velocity dispersion and/or temperature of the GMC, the resulting $X_{\rm CO}$ values fell by a factor of $\sim$5, comparable to both observed starbursts and the model mergers in this paper. While the simulations in Shetty et al. do not model the physical processes which may simultaneously cause $N_{\rm H_2}$, σ and T to vary, these models do confirm that when increasing σ or T and considering the radiative transfer through clouds, one will observe a depressed $X_{\rm CO}$, as is inferred in ULIRGs.

In this sense, the models of Shetty et al. are complementary to those presented here. Shetty et al.'s models resolve much of the physics and chemistry within GMCs, though they have no information regarding the external environment from the host galaxy and how it may affect the cloud. Our simulations describe the ambient environment surrounding the model GMCs, though at best they resolve the surfaces of the clouds (and require some amount of subresolution techniques). That both sets of models are converging upon the same result from different directions is encouraging. The next step forward will be to fully couple galaxy evolution simulations with high-resolution models of GMCs with a grid of model GMCs. These efforts are underway and will be presented in due course (Feldmann et al., in preparation; Narayanan & Shetty, in preparation).

6 SUMMARY AND CONCLUSIONS

Utilizing a combination of hydrodynamic simulations of disc galaxy evolution and galaxy mergers, dust and molecular line radiative transfer calculations, we investigated the dependence of the CO–H_2 conversion factor on galactic environment. Our main results are the following.

(i) Provided that GMCs are gravitationally bound, disc galaxies in the local Universe has relatively little influence on the physical properties of GMCs within them (outside the central $\sim$kpc). The velocity dispersions are typically dominated by internal processes to the GMC, and the temperatures are roughly constant at $\sim$10 K, set by a balance of molecular/atomic line cooling and cosmic ray and grain photoelectric effect heating. In this situation, when the surface densities of GMCs are comparable to those in the Galaxy, $X_{\rm CO}$ will be similar to the Galactic value of $X_{\rm CO} \approx 2$–$4 \times 10^{20}\,{\rm cm^{-2}/K\,km\,s^{-1}}$.

(ii) In galaxy mergers, the GMC physical properties are strongly affected by the galaxy environment. The rise in surface density in GMCs during the merger is offset by an increase in the velocity dispersion coupled to a rise in the kinetic temperature of the gas caused by efficient dust–gas thermal exchange at high densities. The combination of increased velocity dispersion and kinetic temperature increases the CO intensity, and lowers the observed $X_{\rm CO}$ from the Galactic value by a typical factor of $\sim$2–10.

(iii) There is a slight trend with galactocentric radius such that GMCs toward the centres of disc galaxies will have a lower $X_{\rm CO}$ than the disc-averaged value, owing to both increased velocity dispersions in the clouds, as well as higher kinetic temperatures.

ACKNOWLEDGMENTS

This work benefited from discussions had and coding done at the Aspen Center for Physics. DN would like thank Patrik Jonsson for numerous helpful conversations regarding adaptive mesh techniques in radiative transfer modelling, and Rahul Shetty, Andrew Baker, Emanuele Daddi, Robert Feldmann, Adam Leroy, Padelis Papadopoulos and Erik Rosolowsky for sharing their knowledge on $X_{\rm CO}$ in galaxies. As always, T. J. Cox's wisdom was invaluable in understanding the physics associated with galaxy mergers. The authors thank the referee, Simon Glover, for a constructive report. Finally, DN would like to thank Rob Kennicutt for providing the original motivation to pursue this study following an insightful question at the 2007 Gas Accretion and Star Formation Workshop in Garching. DN acknowledges support from the NSF via grant AST-1009452. MK acknowledges support from an Alfred P. Sloan fellowship, the NSF through grants AST-0807739 and CAREER-0955300 and NASA through Astrophysics Theory and Fundamental Physics grant NNX09AK31G and a *Spitzer Space Telescope* Theoretical Research Program grant. ECO acknowledges support from the NSF via grant AST-0908185. The simulations in this paper were run on the Odyssey cluster, supported by the Harvard FAS Research Computing Group.

REFERENCES

Abdo A. A. et al., 2010a, ApJ, 709, L152
Abdo A. A. et al., 2010b, ApJ, 710, 133
Arimoto N., Sofue Y., Tsujimoto T., 1996, PASJ, 48, 275
Barnes J. E., Hernquist L. E., 1991, ApJ, 370, L65
Barnes J. E., Hernquist L., 1996, ApJ, 471, 115
Bell T. A., Roueff E., Viti S., Williams D. A., 2006, MNRAS, 371, 1865
Bell T. A., Viti S., Williams D. A., 2007, MNRAS, 378, 983
Bigiel F., Leroy A., Walter F., Brinks E., de Blok W. J. G., Madore B., Thornley M. D., 2008, AJ, 136, 2846
Blitz L., Rosolowsky E., 2006, ApJ, 650, 933
Blitz L., Fukui Y., Kawamura A., Leroy A., Mizuno N., Rosolowsky E., 2007, in Reipurth B., Jewitt D., Keil K., eds, Protostars and Planets V. Univ. Arizona, Tucson, p. 81
Bloemen J. B. G. M. et al., 1986, A&A, 154, 25
Bolatto A. D., Leroy A. K., Rosolowsky E., Walter F., Blitz L., 2008, ApJ, 686, 948
Boselli A., Lequeux J., Gavazzi G., 2002, Ap&SS, 281, 127
Bouché N. et al., 2007, ApJ, 671, 303
Bournaud F. et al., 2011, ApJ, 730, 4
Calura F., Pipino A., Matteucci F., 2008, A&A, 479, 669
Chakrabarti S., Cox T. J., Hernquist L., Hopkins P. F., Robertson B., Di Matteo T., 2007, ApJ, 658, 840
Cox T. J., Di Matteo T., Hernquist L., Hopkins P. F., Robertson B., Springel V., 2006a, ApJ, 643, 692
Cox T. J., Jonsson P., Primack J. R., Somerville R. S., 2006b, MNRAS, 373, 1013
Cox T. J. et al., 2006c, ApJ, 650, 791
Daddi E. et al., 2005, ApJ, 631, L13
Daddi E. et al., 2007, ApJ, 670, 156

Daddi E. et al., 2010, ApJ, 714, L118
Dalgarno A., McCray R. A., 1972, ARA&A, 10, 375
Dame T. M., Hartmann D., Thaddeus P., 2001, ApJ, 547, 792
Dib S., Bell E., Burkert A., 2006, ApJ, 638, 797
Dickman R. L., 1975, ApJ, 202, 50
Di Matteo T., Springel V., Hernquist L., 2005, Nat, 433, 604
Dobbs C. L., Glover S. C. O., Clark P. C., Klessen R. S., 2008, MNRAS, 389, 1097
Downes D., Solomon P. M., 1998, ApJ, 507, 615
Downes D., Solomon P. M., 2003, ApJ, 582, 37
Draine B. T., Li A., 2007, ApJ, 657, 810
Draine B. T. et al., 2007, ApJ, 663, 866
Dwek E., 1998, ApJ, 501, 643
Evans N. J., II, 1999, ARA&A, 37, 311
Feldmann R., Gnedin N. Y., Kravtsov A. V., 2011, ApJ, 732, 115
Förster Schreiber N. M. et al., 2009, ApJ, 706, 1364
Fumagalli M., Krumholz M. R., Hunt L. K., 2010, ApJ, 722, 919
Genzel R. et al., 2006, Nat, 442, 786
Genzel R. et al., 2010, MNRAS, 407, 2091
Glover S. C. O., Mac Low M.-M., 2011, MNRAS, 412, 337
Glover S. C. O., Federrath C., Mac Low M., Klessen R. S., 2010, MNRAS, 404, 2
Gnedin N. Y., Kravtsov A. V., 2010, ApJ, 714, 287
Gnedin N. Y., Tassis K., Kravtsov A. V., 2009, ApJ, 697, 55
Goldsmith P. F., 2001, ApJ, 557, 736
Groves B. A., Dopita M. A., Sutherland R. S., 2004, ApJS, 153, 9
Groves B., Dopita M. A., Sutherland R. S., Kewley L. J., Fischera J., Leitherer C., Brandl B., van Breugel W., 2008, ApJS, 176, 438
Hayward C. C., Narayanan D., Jonsson P., Cox T. J., Kereš D., Hopkins P. F., Hernquist L., 2010, in Treyer, Lee, Seibert, Wyder, Neil, eds, Conference Proceedings for UP2010: Have Observations Revealed a Variable Upper End of the Initial Mass Function? preprint (arXiv:1008.4584)
Hayward C. C., Kereš D., Jonsson P., Narayanan D., Cox T. J., Hernquist L., 2011, preprint (arXiv:1101.0002)
Hernquist L., 1990, ApJ, 356, 359
Heyer M., Krawczyk C., Duval J., Jackson J. M., 2009, ApJ, 699, 1092
Hinz J. L., Rieke G. H., 2006, ApJ, 646, 872
Hollenbach D. J., Tielens A. G. G. M., 1999, Rev. Modern Phys., 71, 173
Hopkins P. F., Hernquist L., 2010, MNRAS, 402, 985
Hopkins P. F. et al., 2005a, ApJ, 625, L71
Hopkins P. F. et al., 2005b, ApJ, 630, 705
Hopkins P. F. et al., 2006, ApJS, 163, 1
Hopkins P. F., Richards G. T., Hernquist L., 2007a, ApJ, 654, 731
Hopkins P. F., Lidz A., Hernquist L., Coil A. L., Myers A. D., Cox T. J., Spergel D. N., 2007b, ApJ, 662, 110
Hopkins P. F. et al., 2008a, ApJ, 679, 156
Hopkins P. F. et al., 2008b, ApJS, 175, 356
Hopkins P. F. et al., 2008c, ApJS, 175, 390
Hopkins P. F., Cox T. J., Hernquist L., 2008d, ApJ, 689, 17
Hopkins P. F. et al., 2009, ApJS, 181, 135
Hopkins P. F., Younger J. D., Hayward C. C., Narayanan D., Hernquist L., 2010, MNRAS, 402, 1693
Israel F. P., 2005, A&A, 438, 855
Jonsson P., 2006, MNRAS, 372, 2
Jonsson P., Primack J. R., 2010, New Astron., 15, 509
Jonsson P., Groves B. A., Cox T. J., 2010, MNRAS, 186
Joung M. R., Mac Low M., Bryan G. L., 2009, ApJ, 704, 137
Juneau S., Narayanan D. T., Moustakas J., Shirley Y. L., Bussmann R. S., Kennicutt R. C., Vanden Bout P. A., 2009, ApJ, 707, 1217
Juvela M., 2005, A&A, 440, 531
Kennicutt R. C., Jr, 1998a, ARA&A, 36, 189
Kennicutt R. C., Jr, 1998b, ApJ, 498, 541
Kennicutt R. C., Jr et al., 2003, PASP, 115, 928
Krumholz M. R., Gnedin N. Y., 2011, ApJ, 729, 36
Krumholz M. R., Thompson T. A., 2007, ApJ, 669, 289
Krumholz M. R., Matzner C. D., McKee C. F., 2006, ApJ, 653, 361
Krumholz M. R., McKee C. F., Tumlinson J., 2008, ApJ, 689, 865
Krumholz M. R., McKee C. F., Tumlinson J., 2009a, ApJ, 693, 216
Krumholz M. R., McKee C. F., Tumlinson J., 2009b, ApJ, 699, 850
Krumholz M. R., Leroy A. K., McKee C. F., 2011, ApJ, 731, 25
Kutner M. L., Leung C. M., 1985, ApJ, 291, 188
Larson R. B., 1981, MNRAS, 194, 809
Lee H., Bettens R. P. A., Herbst E., 1996, A&AS, 119, 111
Leech J., Isaak K. G., Papadopoulos P. P., Gao Y., Davis G. R., 2010, MNRAS, 406, 1364
Le Floc'h E. et al., 2005, ApJ, 632, 169
Lemaster M. N., Stone J. M., 2008, ApJ, 682, L97
Leroy A., Bolatto A., Walter F., Blitz L., 2006, ApJ, 643, 825
Leroy A. K. et al., 2011, ApJ, 737, 12
Liszt H. S., Pety J., Lucas R., 2010, A&A, 518, A45
McKee C. F., Krumholz M. R., 2010, ApJ, 709, 308
McKee C. F., Ostriker J. P., 1977, ApJ, 218, 148
McKee C. F., Ostriker E. C., 2007, ARA&A, 45, 565
Maloney P., Black J. H., 1988, ApJ, 325, 389
Mao R., Schulz A., Henkel C., Mauersberger R., Muders D., Dinh-V-Trung, 2010, ApJ, 724, 1336
Meier D. S., Turner J. L., Beck S. C., Gorjian V., Tsai C., Van Dyk S. D., 2010, AJ, 140, 1294
Mihos J. C., Hernquist L., 1994, ApJ, 431, L9
Mihos J. C., Hernquist L., 1996, ApJ, 464, 641
Mo H. J., Mao S., White S. D. M., 1998, MNRAS, 295, 319
Mühle S., Henkel C., de Maio T., Seaquist E. R., 2011, preprint (arXiv:1101.1262)
Narayanan D., Groppi C. E., Kulesa C. A., Walker C. K., 2005, ApJ, 630, 269
Narayanan D. et al., 2006a, ApJ, 642, L107
Narayanan D., Kulesa C. A., Boss A., Walker C. K., 2006b, ApJ, 647, 1426
Narayanan D., Cox T. J., Hernquist L., 2008a, ApJ, 681, L77
Narayanan D. et al., 2008b, ApJS, 176, 331
Narayanan D., Cox T. J., Shirley Y., Davé R., Hernquist L., Walker C. K., 2008c, ApJ, 684, 996
Narayanan D., Cox T. J., Hayward C. C., Younger J. D., Hernquist L., 2009, MNRAS, 400, 1919
Narayanan D., Hayward C. C., Cox T. J., Hernquist L., Jonsson P., Younger J. D., Groves B., 2010a, MNRAS, 401, 1613
Narayanan D. et al., 2010b, MNRAS, 407, 1701
Noeske K. G. et al., 2007a, ApJ, 660, L43
Noeske K. G. et al., 2007b, ApJ, 660, L47
Obreschkow D., Rawlings S., 2009, ApJ, 696, L129
Obreschkow D., Croton D., De Lucia G., Khochfar S., Rawlings S., 2009, ApJ, 698, 1467
Offner S. S. R., Klein R. I., McKee C. F., Krumholz M. R., 2009, ApJ, 703, 131
Oka T., Hasegawa T., Hayashi M., Handa T., Sakamoto S., 1998, ApJ, 493, 730
Ostriker E. C., Shetty R., 2011, ApJ, 731, 41
Ostriker E. C., Stone J. M., Gammie C. F., 2001, ApJ, 546, 980
Ostriker E. C., McKee C. F., Leroy A. K., 2010, ApJ, 721, 975
Padoan P., Nordlund Å., 2002, ApJ, 576, 870
Papadopoulos P. P., 2010, ApJ, 720, 226
Papadopoulos P. P., Thi W., Miniati F., Viti S., 2011, MNRAS, 414, 1705
Pelupessy F. I., Papadopoulos P. P., 2009, ApJ, 707, 954
Pelupessy F. I., Papadopoulos P. P., van der Werf P., 2006, ApJ, 645, 1024
Pety J., Liszt H. S., Lucas R., 2011, preprint (arXiv:1102.4667)
Price D. J., Federrath C., Brunt C. M., 2011, ApJ, 727, L21
Robertson B. E., Kravtsov A. V., 2008, ApJ, 680, 1083
Robertson B., Yoshida N., Springel V., Hernquist L., 2004, ApJ, 606, 32
Robertson B. et al., 2006, ApJ, 641, 21
Rosolowsky E., Engargiola G., Plambeck R., Blitz L., 2003, ApJ, 599, 258
Schöier F. L., van der Tak F. F. S., van Dishoeck E. F., Black J. H., 2005, A&A, 432, 369
Scoville N. Z., Yun M. S., Bryant P. M., 1997, ApJ, 484, 702
Shetty R., Ostriker E. C., 2008, ApJ, 684, 978
Shetty R., Glover S. C., Dullemond C. P., Klessen R. S., 2011a, MNRAS, 412, 1686

Shetty R., Glover S. C., Dullemond C. P., Ostriker E. C., Harris A. I., Klessen R. S., 2011b, MNRAS, 415, 3253
Snyder G. F., Cox T. J., Hayward C. C., Hernquist L., Jonsson P., 2011, preprint (arXiv:1102.3689)
Solomon P. M., Rivolo A. R., Barrett J., Yahil A., 1987, ApJ, 319, 730
Solomon P. M., Downes D., Radford S. J. E., Barrett J. W., 1997, ApJ, 478, 144
Springel V., 2000, MNRAS, 312, 859
Springel V., 2005, MNRAS, 364, 1105
Springel V., Hernquist L., 2002, MNRAS, 333, 649
Springel V., Hernquist L., 2003, MNRAS, 339, 289
Springel V., Di Matteo T., Hernquist L., 2005a, ApJ, 620, L79
Springel V., Di Matteo T., Hernquist L., 2005b, MNRAS, 361, 776
Sternberg A., Dalgarno A., 1995, ApJS, 99, 565
Strong A. W., Mattox J. R., 1996, A&A, 308, L21
Tacconi L. J. et al., 2008, ApJ, 680, 246
Tan J. C., 2000, ApJ, 536, 173
Teyssier R., Chapon D., Bournaud F., 2010, ApJ, 720, L149
van Zadelhoff G. et al., 2002, A&A, 395, 373
Vladilo G., 1998, ApJ, 493, 583
Walker C. K., Narayanan G., Boss A. P., 1994, ApJ, 431, 767
Wall W. F., 2007, MNRAS, 379, 674
Weingartner J. C., Draine B. T., 2001, ApJ, 548, 296
Wilson C. D., 1995, ApJ, 448, L97
Wolfire M. G., Hollenbach D., McKee C. F., 2010, ApJ, 716, 1191
Xu X., Narayanan D., Walker C., 2010, ApJ, 721, L112
Yao L., Seaquist E. R., Kuno N., Dunne L., 2003, ApJ, 588, 771
Younger J. D., Hayward C. C., Narayanan D., Cox T. J., Hernquist L., Jonsson P., 2009, MNRAS, 396, L66

APPENDIX A: EFFECTS OF PARAMETER CHOICES AND ASSUMPTIONS

In Section 2, we outlined a number of parameter choices which could potentially influence the results in this paper. Here, we discuss the results in the context of these assumptions.

A1 Self-consistency of the temperature calculations

First, there is a discrepancy between the way the dust temperature is calculated in SUNRISE and in our temperature equilibrium model. In the former, the dust temperature is assumed to be in equilibrium with the radiation field, but we do not take into account any thermal exchange between the gas and dust. In the temperature equilibrium model, the dust grains are assumed to be able to exchange energy with the gas, but we hold the ambient radiation field fixed, rather than allowing it to change as the dust temperature does. Given the importance of the dust temperature in raising the gas temperature in this model, it is worth investigating any potential differences between the two dust temperatures.

In Fig. A1, we plot the ratio of $T_{\rm dust}$ from SUNRISE compared to $T_{\rm dust}$ from the temperature equilibrium model as a function of GMC density[9] for our fiducial merger. There is generally good agreement between the two, though some number of points at higher densities deviate strongly from unity. The gas which has poor agreement between the two dust temperature calculations almost exclusively has all of its carbon in atomic form, rather than molecular. Beyond this, this gas tends to be towards the outskirts of the galaxy, in rather large cells in the adaptive mesh with relatively low masses ($\sim$10 $M_\odot$). Because we enforce a rule that clouds must have a minimum surface density of 100 $M_\odot$ pc^{-2}, these regions have extremely high densities, even if relatively low mass. In atomic gas of this density, the gas couples with the dust and can cause the dust temperature to change from that of the background radiation field. These outlying points have little effect on the final results, however, as they contain rather little mass. We denote the 95th mass percentile by the blue shaded region in Fig. A1. That is, the sum of the mass in the points outside of the blue region accounts for <5 per cent of the total molecular mass in the galaxy. As is shown, the differences in the two dust temperatures are small in this shaded region.

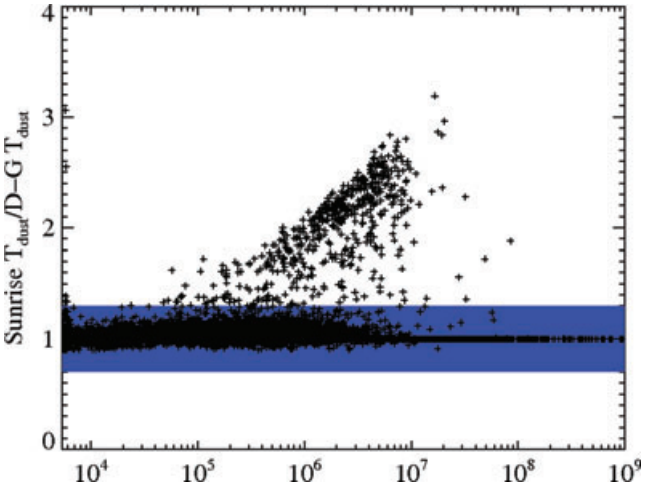

Figure A1. Comparison between the SUNRISE dust temperatures and those calculated from the temperature equilibrium calculation as a function of density for model GMCs in our fiducial merger. See text for details.

A2 SUNRISE input parameters

Similarly, a number of our assumptions in the SUNRISE modelling can have an effect on the derived dust temperature. We investigate those here. The important figure for these tests is Fig. A2. Referring to Section 2.3, the time-averaged covering fraction of birthclouds around stellar clusters is a free parameter. While we chose a modest covering fraction, it is possible that a larger fraction may be

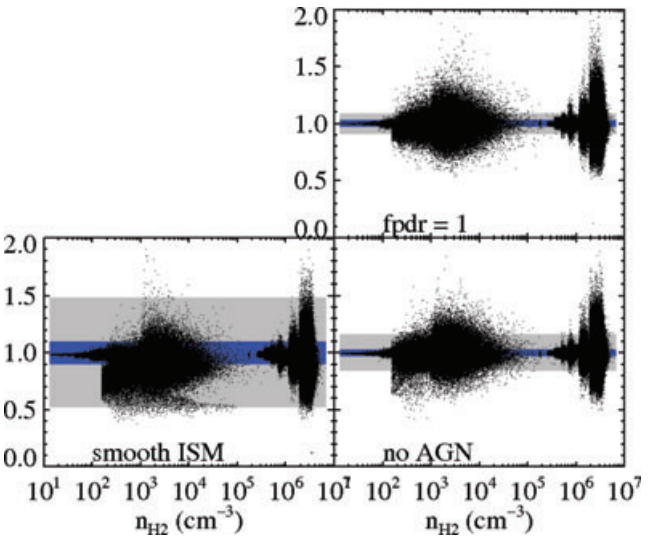

Figure A2. Ratio of $T_{\rm dust}$ under various subresolution ISM specifications to that derived in our fiducial model versus H_2 density in model GMCs. See text for details.

[9] This is not the actual mean density of the GMC, but the density accounting for an enhancement by the turbulent compression of gas. This is the density that is used in the temperature equilibrium calculation.

reasonable. For example, if we choose a fraction $f_{\rm PDR} = 1$, the O and B stars would be blanketed by the ISM for their entire lives. This situation may exist in ULIRGs. To test for the effect in varying $f_{\rm PDR}$, we plot the ratio of the dust temperatures derived from SUNRISE for a model with $f_{\rm PDR} = 1$ over the dust temperature from our fiducial model with $f_{\rm PDR} = 0.3$ against GMC density. The blue shaded region shows the 95th mass percentile, and grey denotes the 99th mass percentile. The model with a larger clearing time-scale for the birthclouds has cooler dust temperatures as less UV flux interacts with the ISM. However, the differences in dust temperature are generally within a factor of 50 per cent, and much less than that (<10 per cent) when considering the bulk of the mass of the galaxy. We conclude that the PDR covering fraction is not an important driver in our model results.

We can explore the effect of discarding the PDR birthcloud model, and assuming the cold ISM has a uniform volume-filling fraction. In this case, the UV photons escape the star particles easily, though optical depths for the photons in the ISM are large. For some number of the clouds outside of the nuclear region, the dust temperatures are thus colder than in our fiducial model (the low ratio points in Fig. A2). However, the bulk of the gas mass is in a confined nuclear region in the galaxy which sees the intense UV radiation field. Because of this, this dust is heated well, and has comparable dust temperatures to our fiducial model. The dispersion in dust temperatures is again within 50 per cent, and the 95th percentile of mass shows relatively small discrepancies.

It is possible that the AGN in the model merger contributes strongly to the dust temperature. To test this, we investigate a model where we have turned off the contribution of the AGN in determining the dust temperature in the merger. While it is difficult to see by eye, the dust temperatures in the model with the AGN are hotter than the model with no AGN. By and large, however, the AGN is not powerful enough to have a significant effect on the overall temperature structure of the cold ISM as noted by the blue and grey shaded regions.

A3 GADGET-3 input parameters

We now turn to possible parameters in the hydrodynamics simulations which may affect our results. As described in Section 2.1, we make a number of parameter choices which may affect the star formation history of the model galaxies. Because the gas densities and dust and gas temperature can depend on these assumptions, it is worth exploring the robustness of our model results in the context of these choices.

There are two principal parameter choices which govern the physical state of the ISM in our hydrodynamic modes: the star formation 'law', and the EOS. As discussed in Section 2.1, we adopt a star formation law such that the star formation time-scale is assumed to be proportional to the local dynamical time-scale, and whose rate matches the normalization of the locally observed Kennicutt (1998a) relation.

In the absence of a complete theory of star formation, a number of possible choices exist regarding the implementation of a star formation recipe on subresolution scales. One can imagine a similar KS solution, though with an index of unity as appears to be observed on resolved scales in nearby galaxies (Bigiel et al. 2008), or steeper index as tentative observational (Bouché et al. 2007) and theoretical (Feldmann, Gnedin & Kravtsov 2011) evidence motivates at high redshift. Beyond this, more sophisticated physical models may provide reasonable prescriptions for star formation in galaxy evolution models (e.g. Tan 2000; Krumholz, McKee & Tumlinson 2009b; Ostriker et al. 2010). While it is outside the scope of this study to perform a detailed study of various star formation recipes in GADGET-3, we perform some simple tests to investigate the role of our adopted star formation law in driving the simulated $X_{\rm CO}$ factors.

Table A1. Variation of mean $X_{\rm CO}$ with different hydrodynamic or subresolution assumptions.

Model	Mean $X_{\rm CO}$ ($\rm cm^{-2}/K\,km\,s^{-1}$)
Fiducial	6.31×10^{19}
Stiff EOS	1.08×10^{20}
KS = 2	5.43×10^{19}
KS = 1	2.73×10^{20}
OML G-scaling	7.10×10^{19}
Half-res	3.02×10^{19}

In Table A1, we show the luminosity-weighted mean $X_{\rm CO}$ values for our fiducial merger during the peak of their starburst for a variety of input parameters in our GADGET-3 simulations. The KS index = 2 case shows a comparable $X_{\rm CO}$ value as the fiducial merger. While the burst is moderately diminished (owing to rapid consumption of the gas during early phases of the merger's evolution, though still quite large at $\sim$250 $\rm M_\odot\,yr^{-1}$ as opposed to $\sim$340 $\rm M_\odot\,yr^{-1}$ in the fiducial merger), the large stellar mass upon coalescence maintains a large velocity dispersion in the gas. This drives a low mean $X_{\rm CO}$.

The model with the largest impact on our results is the model with KS index = 1. This model merger has a mean $X_{\rm CO}$ comparable to the model disc. Models with a KS index of 1 do not go through a burst upon merging (Cox, private communication). With a KS index of 1, to first order, the total SFR is proportional to the total gas mass. Because we do not include any gas replenishment from the intergalactic medium, the gas mass only decreases with time, as does the SFR in this simulation. The low SFR upon merging leads to low gas/dust temperatures, and increased $X_{\rm CO}$. We note that this situation is unlikely to describe real mergers as, observationally, galaxy mergers exhibit the highest SFRs in the local Universe. Both observational (Bigiel et al. 2008) and theoretical (Krumholz et al. 2009b; Ostriker & Shetty 2011) evidence suggest that a KS index >1 may describe high surface density systems.

We utilize an EOS for the ISM which incorporates a subresolution prescription for capturing the effect of supernovae heating of the ISM (Springel & Hernquist 2003). The nominal Springel & Hernquist (2003) and Springel et al. (2005b) EOS is given by

$$P_{\rm eff} = (\gamma - 1)(\rho_{\rm h} u_{\rm h} + \rho_{\rm c} u_{\rm c}), \quad \text{(A1)}$$

where $\gamma = 5/3$ as the adiabatic index of the gas, $\rho_{\rm h,c}$ is the density of the hot and cold phase and $u_{\rm h,c}$ is the specific thermal energy of the two phases. For a given initial mass function (IMF), Springel & Hernquist (2003) show that the EOS is completely defined by the star formation time-scale, the normalization of the cloud evaporation rate and a supernovae 'temperature' which defines the heating rate from supernovae of a given IMF. The full 'effective' EOS has the property in which pressure rises with density faster than an isothermal gas, as can be seen in fig. 4 of Springel et al. (2005b).

Our fiducial model utilizes a softer EOS than the full model. In particular, we interpolate between the full 'stiff' model (where we assign a parameter $q_{\rm EOS} = 1$) and isothermal model ($q_{\rm EOS} = 0$) and employ $q_{\rm EOS} = 0.25$. In the full 'stiff' EOS as in simulations of discs scaled for the local Universe, the ISM can become so pressurized as to appear smooth with relatively few clumps (Springel et al. 2005b).

To test our assumption of a softer EOS, we have run a test simulation with $q_{\rm EOS} = 1$.

In Table A1, we show the mean $X_{\rm CO}$ for our fiducial merger, though with $q_{\rm EOS} = 1$ (denoted 'stiff EOS'). We see a larger value than the fiducial model. Isolating the root cause is non-trivial. By effectively increasing the effect of supernovae feedback, we increase dust heating (by reducing the clumpiness of the gas), though we also reduce the magnitude of the burst (due to a retardation of gas fragmentation). These effects serve to somewhat offset one another with respect to the gas temperature.

We test whether our assumption of $G_0 = 1$ outside of clouds plays a strong role in our model results. Following Ostriker et al. (2010), we have run a model in which we scale the interstellar radiation field by the value of the local SFR compared to that in the solar neighbourhood, and show the mean $X_{\rm CO}$ value in Table A1 (denoted by 'OML G-scaling'). Because the clouds are strongly shielded in this model, scaling G makes little difference.

Finally, we consider the spatial resolution of our model. Our current resolution has cell sizes ($\sim$70 pc) which are of order the SPH smoothing length. Further increasing the spatial resolution does not provide new physical information. More seriously, increasing the spatial resolution of the SPH simulations would run into scenarios of unphysical descriptions of the ISM with the Springel & Hernquist (2003) multiphase model. We can see, however, what direction the results may go if it were possible to increase our resolution. To investigate this, we have run our fiducial merger snapshot with one less level of refinement in the adaptive mesh, giving a minimum cell size of $\sim$140 pc, and show the mean $X_{\rm CO}$ in Table A1 (denoted by 'half-res'). The mean $X_{\rm CO}$ in the low-resolution model is 60 per cent the value of the fiducial model. It is conceivable, then, that further increasing the spatial resolution would increase $X_{\rm CO}$ in the merger model. On the other hand, reducing the cell size would result in more resolved GMCs. Because it is the resolved GMCs that drive the mean $X_{\rm CO}$ for the merger model, it is also possible that increased spatial resolution would result in little change to the results presented here.

This paper has been typeset from a TEX/LATEX file prepared by the author.